

Sedimentary mechanisms of a modern banded iron formation on
Milos Island, Greece

^{1,2}Ernest Chi Fru*, ³Stephanos Kiliass, ^{4,5}Magnus Ivarsson, ¹Jayne E. Rattray,
³Katerina Gkika, ²Iain McDonald, ⁶Qian He, ¹Curt Broman

¹Department of Geological Sciences, 10691, Stockholm University, Sweden.

²School of Earth and Ocean Sciences, Cardiff University, Park Place, CF10 3AT,
Cardiff, UK.

³Department of Economic Geology and Geochemistry, Faculty of Geology and
Geoenvironment, National and Kapodistrian University of Athens, Panepistimiopolis,
Zographou, 15784, Athens, Greece.

⁴Department of Biology, University of Southern Denmark, Campusvej 55, Odense M,
DK5230, Denmark

⁵Department of Palaeobiology, Swedish Museum of Natural History, Box 50007,
Stockholm, Sweden.

⁶School of Chemistry, Cardiff University, Park Place, CF10 3AT, Cardiff, UK.

*Corresponding author

Tel: +44(0) 29 208 70058

Email: ChiFruE@cardiff.ac.uk

Short title: A modern banded iron formation

Abstract. An Early Quaternary shallow submarine hydrothermal iron formation (IF) in the Cape Vani sedimentary basin (CVSB) on Milos Island, Greece, displays banded rhythmicity similar to Precambrian banded iron formation (BIF). Field-wide stratigraphic and biogeochemical reconstruction show two temporal and spatially isolated iron deposits in the CVSB with distinct sedimentological character. Petrographic screening suggests the photoferrotrophic-like microfossil-rich IF (MFIF), accumulated on a basement consisting of andesites, in a ~150 m wide basin, in the SW margin of the basin. A banded non-fossiliferous IF (NFIF) sits on top of the Mn-rich sandstones at the transition to the renowned Mn-rich formation, capping the NFIF unit. Geochemical data relates the origin of the NFIF to periodic submarine volcanism and water column oxidation of released Fe(II) in conditions predominated by anoxia, similar to the MFIF. Raman spectroscopy pairs hematite-rich grains in the NFIF with relics of a carbonaceous material carrying an average $\delta^{13}\text{C}_{\text{org}}$ signature of ~-25‰. A similar $\delta^{13}\text{C}_{\text{org}}$ signature in the MFIF could not be directly coupled to hematite by mineralogy. The NFIF, which post dates large-scale Mn deposition in the CVSB, is composed primarily of amorphous Si (opal-SiO₂·nH₂O) while crystalline quartz (SiO₂) predominates the MFIF. An intricate interaction between tectonic processes, changing redox, biological activity and abiotic Si precipitation are proposed to have collectively formed the unmetamorphosed BIF-type deposits in a shallow submarine volcanic center. Despite the differences in Precambrian ocean-atmosphere chemistry and the present geologic time, these formation mechanisms coincide with those believed to have formed Algoma-type BIFs proximal to active seafloor volcanic centers.

Keywords: Banded iron formation; BIF analog; Hydrothermal activity; Iron cycling; Silica cycling.

64 **1 Introduction**

65 Banded iron formations (BIF) are chemical marine sediments of Precambrian origin
 66 (Bekker et al., 2010). They contain at least 15% bulk Fe content and are characterized
 67 by spectacular Fe-rich bands alternating with cherty Si-rich layers (James, 1954;
 68 Gross, 1980; Simonson, 1985, 2003; Bekker et al., 2010). The interval spanning
 69 3800-1800 million years ago (Ma), records intermittent but widespread BIF
 70 deposition on all continents. After a ~1000 million year hiatus, BIFs reappeared
 71 briefly during the Neoproterozoic Snowball Earth glaciations, ~750-550 Ma
 72 (Hoffman et al., 1998; Bekker et al., 2010). BIFs are therefore considered a unique
 73 feature of a distinct Precambrian ocean-atmosphere chemistry, compared to the fully
 74 oxygenated Phanerozoic ocean and atmosphere (Bekker et al., 2010; Poulton and
 75 Canfield, 2011).

76 Recently, a curious ~2.0 million year old Early Quaternary iron formation (IF)
 77 displaying banded rhythmicity typical of BIFs, was serendipitously discovered in the
 78 Cape Vani Sedimentary Basin (CVSB), Milos Island, Greece (Chi Fru et al., 2013,
 79 2015). Before this discovery, Cape Vani was long known to host Mn oxide ores of
 80 economic potential (Hein et al., 2000; Liakopoulos et al., 2001; Glasby et al., 2005;
 81 Kiliass et al., 2007). Milos is an emergent volcano on the Hellenic Volcanic Arc
 82 (HVA) where arc-volcanism and seafloor hydrothermal activity occur in thinned pre-
 83 Alpine to Quaternary continental crust (Kiliass et al., 2013b) (Fig. 1). The first
 84 reported IF from CVSB is unmetamorphosed and contains diverse microfossils
 85 encrusted by hematite, with ferrihydrite proposed as a primary precursor mineral (Chi
 86 Fru et al., 2013, 2015). Field stratigraphy, rare earth elements (REE), stable isotopes,
 87 petrographic and microfossil studies point to microbial Fe deposition in a semi-

enclosed, shallow submarine basin under conditions analogous to those that formed the Precambrian Algoma-type BIFs near volcanic centers (Chi Fru et al., 2015). These earlier reports assumed a one-time basin-wide depositional event and a common origin for all Fe-rich sedimentary rocks in the CVSB.

However, it remains unclear what sedimentary processes caused the distinct deposition of the BIF-type rocks in a basin where Mn precipitation was apparently widespread at various intervals. Moreover, it is not known how the Mn ores relate temporally and spatially to Fe deposition in the ~1 km long CVSB. This knowledge may provide clues to processes that triggered large-scale deposition of similar Proterozoic Fe-Mn-rich deposits (Roy, 2006; Tsikos et al., 2010; Beukes et al., 2016). Here, new sedimentological, petrological and biogeochemical analyses describe cycles of periodic precipitation of shallow submarine Si and Fe-rich sedimentary rocks and the plausible mechanisms that enabled their temporal and spatial separation from the Mn deposits in the CVSB. The data reveal a much more complex depositional system not only controlled by microbial Fe(II) oxidation as previously proposed (Chi Fru et al., 2013, 2015), but suggests episodic submarine hydrothermal activity coupled to changing redox conditions as a central mechanism in the formation of the banded iron rocks.

1.1 Geological setting

K-Ar radiometric dating of biotite and amphiboles belonging to the dacitic/andesitic lava domes flooring the CVSB basin gave an Upper Pliocene age of 2.38 ± 0.1 Ma (Fytikas et al., 1986; Stewart and McPhie, 2006). Similarly, the presence of the gastropod mollusk, *Haustator biplicatus* (Bronn, 1831), in the fossiliferous

sandstones/sandy tuffs hosting the Mn-rich deposit, indicate a biostratigraphic Upper Pliocene to Lower Pleistocene age.

The geology, Fe and Mn mineralization of the CVSB have previously been described in detail (Plimer, 2000; Hein et al., 2000; Liakopoulos et al., 2001; Skarpelis and Koutles, 2004; Glasby et al., 2005; Stewart and McPhie, 2006; Kiliass, 2011; Alfieris and Voudouris, 2005; Alfieris, 2006; Alfieris et al., 2013; Chi Fru et al., 2013, 2015; Papavassiliou et al., 2017). Briefly, the Milos IF is part of the CVSB, a recently emergent sedimentary rift basin located NW of Milos Island, along the HVA in the Aegean Sea, Greece (Fig. 1). It hosts a fossil analog of active shallow-submarine hydrothermal activity on the coast of Milos Island (Dando et al., 1995). The CVSB developed within a shallow-submarine rhyolitic-dacitic volcanic center, filled up mainly by a ~35-50 m thick stratigraphic succession of volcanoclastic/epiclastic sandstones/sandy tuffs, 35-40% of which is hydrothermally mineralized by Mn oxides and barite (Hein et al., 2000; Liakopoulos et al., 2001; Skarpelis and Koutles, 2004; Papavassiliou et al., 2017). Sedimentologic and fossil data (trace, bivalves, echinoid and brachiopod fossils, together with microbially induced sedimentary structures (e.g. Kiliass, 2011)), suggest that most of the CVSB sandstones/sandy tuffs hosting the Mn-rich deposit, are foreshore to shoreface shallow submarine deposits, formed at a maximum depth of 200 mbsl. Over the last 0.8 Myr, fluctuating water depths due to sea-level change of up to 120 m and volcanic edifice building, has resulted in tectonic uplift of ~250 m (Papanikolaou et al., 1990). The CVSB infill, currently 35 m above sea level, is tectonically bound by extrusive rhyolite to the north, framed by elevated andesitic-dacitic centers, with the Cape Vani and the Katsimoutis dacitic lava domes being the most prominent (Fig. 1).

136

137 **2 Methodology**

138 **2.1 Sample preparation**

139 Prior to mineralogical and geochemical analysis, exposed rock surface layers were
140 sawn and removed. GeoTech Labs (Vancouver, Canada) produced doubly polished
141 thin sections for mineralogical and textural analysis. Trace and rare earth element
142 analysis was performed after digestion of powdered samples with a mixture of acids
143 (HNO₃, HCl, HF) and heat until a clear solution was obtained (Chi Fru et al., 2013,
144 2015).

145

146 **2.2 Mineralogical analysis**

147 **2.2.1 X-Ray Diffraction (XRD) analysis**

148 A PANalytical Xpert-pro diffractometer at room temperature, 45 kV, 40 mA and
149 1.5406 Å wavelength and Cu-Kα radiation and Ni-filter, was used for Powder X-Ray
150 Diffraction (PXRD) analysis. Samples were analyzed between 5-80° in step sizes of
151 0.017° with continuous mode scanning step time of 50.1650 s while rotating.

152

153 **2.2.2 Raman spectroscopy**

154 Raman analysis was performed with a confocal laser Raman spectrometer (Horiba
155 instrument LabRAM HR 800), equipped with a multichannel air-cooled (-70°C) 1024
156 x 256 pixel charge-coupled device (CCD) array detector as previously described (Chi
157 Fru et al. 2013, 2015). Spectral resolution was ~0.3 cm⁻¹/pixel. Accuracy was
158 determined by a repeated silicon wafer calibration standard at a characteristic Raman
159 line of 520.7 cm⁻¹.

160

2.2.3 Transmission electron microscopy

Specimens for transmission electron microscopy (TEM) were prepared from the crushed rock specimen powder. This was followed by dry-dispersal onto a 300 mesh holey carbon TEM Cu grid. Microscopy was conducted using a JEOL 2100 TEM with a LaB₆ source in the School of Chemistry, Cardiff University, operated at 200kV. The X-EDS analysis was performed with an Oxford Instrument SDD detector X-Max^N 80 T.

2.2.4 Scanning electron microscopy

Scanning Electron Microscopy-Energy Dispersive Spectroscopy (SEM-EDS) analysis was done on a FEI QUANTA FEG 650 ESEM. Images were captured at 5 kV and EDS data collected at 20 kV, using an Oxford T-Max 80 detector (Oxford Instruments, UK). The analyses were performed in low vacuum to minimize surface charging of uncoated samples. EDS elemental maps were collected for 30 min or until the signal had stabilized, indicated by a clear distribution trend. The data were further processed with the Oxford Aztec software.

2.3 Geochemical analysis

2.3.1 Laser ablation ICP-MS and trace element analysis

Laser Ablation-Inductively Coupled Plasma-Mass Spectrometry (LA-ICP-MS) was performed at Cardiff University on polished thin sections. The LA-ICP-MS system comprised a New Wave Research UP213 laser system coupled to a Thermo X Series 2 ICP-MS. The laser was operated using a frequency of 10 Hz at pulse energy of ~5mJ for an 80µm diameter beam using lines drawn perpendicular to the layering and at a movement speed of 26 microns sec⁻¹. Samples were analyzed in time resolved

analysis (TRA) mode using acquisition times of between 110 and 250 seconds; comprising a 20 second gas blank, 80-220 second ablation and 10 second washout. Dwell times varied from 2 msec for major elements to 35 msec for low abundance trace elements. Blank subtraction was carried out using the Thermo Plasmalab software before time resolved data were exported to Excel.

Separated and independently pulverized banded layers were digested by lithium borate fusion followed by major, trace and rare earth element (REE) analyses using ICP- Atomic Emission Spectrometry-Mass Spectrometry (ICP-AES-MS) and X-Ray Florescence (XRF) at Bureau Veritas (Ankara). Geochemical data were compared with previously published results for the more widely investigated Mn deposits (Hein et al., 2000; Liakopoulos et al., 2001; Glasby et al., 2005).

2.3.2 Isotope analysis

C, N and S isotopic composition for the pulverized samples was determined as previously described (Chi Fru et al., 2013, 2015), following combustion in a Carlo Erba NC2500 analyzer and analyzed in a Finnigan MAT Delta V mass spectrometer, via a split interface to reduce gas volume. Reproducibility was calculated to be better than 0.15‰ for $\delta^{13}\text{C}$ and $\delta^{15}\text{N}$ and 0.2‰ for $\delta^{34}\text{S}$. Total C and N concentrations were determined simultaneously when measuring the isotope ratios. The relative error was <1% for both measurements. For carbon isotopic composition of organic carbon, samples were pre-treated with concentrated HNO_3 prior to analysis.

2.4 Organic geochemistry analysis

Lipid biomarker and compound specific $\delta^{13}\text{C}$ analyses were executed on powdered samples of sectioned bands from which exposed surface layers had been removed.

211 Modern sediments from Spathi Bay, 36°40'N, 24°31'E, southeast of Milos Island,
212 collected by push coring at 12.5 m below the seafloor were freeze-dried prior to
213 extraction to aid the identification of potential syngenetic biomarkers in the
214 Quaternary rocks. Between 4-6 g of ground samples were ultrasonically extracted
215 using 3×Methanol, 3×(1:1) Methanol:Dichloromethane (DCM), and 3×DCM and
216 extracts were combined and dried under N₂. Samples were subsequently re-dissolved
217 in DCM then methylated following the method of Ichihara and Fukubayashi (2010).
218 The resulting residue was silylated using, 20 µl pyridine and 20 µl (N, O-
219 Bis(trimethylsilyl)trifluoroacetamide) BSTFA and heated at 60°C for 15 min. Total
220 lipid extracts were analyzed using a Shimadzu QP 2010 Ultra gas chromatography
221 mass spectrometer (GC/MS). Separation was performed on a Zebron ZB-5HT column
222 (30 m x 0.25 mm x 0.10 µm) with a helium carrier gas flow at 1.5 ml min⁻¹. Samples
223 were injected splitless, onto the column at 40°C with the subsequent oven temperature
224 program ramped to 180°C at a rate of 15°C min⁻¹, followed by ramping to 325°C at a
225 rate of 4°C min⁻¹ and a final hold for 15 min. The MS was set to scan from 50 to 800
226 m/z with an event time of 0.70 sec and a scan speed of 1111 u/sec. All peaks were
227 background subtracted and identification confirmed using the NIST GC/MS library
228 and literature spectra. Contamination was not introduced into the samples, as blank
229 samples worked up concurrently with the rock fractions had results comparable to the
230 ethyl acetate instrument blank.

231

232 **2.5 Chemical weathering analysis**

233 Chemical index of alternation (CIA) was used to determine whether variations in
234 chemical weathering intensities would in addition to hydrothermal activity deliver
235 materials into the depositional basin from the continent, according to the

236 formula: $CIA = Al_2O_3 / (Al_2O_3 + CaO + Na_2O + K_2O) \times 100$. Extensively
 237 applied, the CIA index reveals subtle changes in weathering fluxes (Nesbit and
 238 Young, 1982; Maynard, 1993; Bahlburg & Dobrzinski, 2011), where increasing CIA
 239 values generally indicate amplified chemical dissolution of rocks and selective release
 240 of dissolvable CaO, Na₂O and K₂O into solution (Nesbit & Young, 1982; Maynard,
 241 1993; Bahlburg & Dobrzinski, 2011). The broken rock particles enriched in the
 242 poorly soluble Al₂O₃ fraction, settle to the seafloor as weathered sediments carrying a
 243 chemical composition different from the source. In the absence of chemical
 244 dissolution, no net chemical change is expected in the composition of sediments
 245 compared to source and thus a low CIA index. CIA indices for detritus of 0-55, 55-75
 246 and >75, are considered unweathered, unweathered to slightly weathered and
 247 weathered to highly weathered, respectively (Nesbit & Young, 1982; Maynard, 1993;
 248 Bahlburg & Dobrzinski, 2011).

249

250 **2.6 Redox analysis**

251 Redox depositional conditions were evaluated using the sequential Fe extraction
 252 redox proxy (Poulton and Canfield, 2005, 2011), combined with REE composition of
 253 the sediment (Planavsky et al., 2010).

254

255 **2.6.1 REE redox analysis**

256 REE data obtained as described in section 2.3.1 were normalized with the North
 257 American Shale Composite (NASC) to maintain consistency with previous studies in
 258 which NASC-normalized REE data (SN) were reported for the Milos BIF-type rocks
 259 (Chi Fru et al., 2013, 2015). The data were further normalized with the Post Archean
 260 Australian Shale (PAAS) (McLennan, 1989) standard for comparative purposes,

according to Bau and Dulski (1996). Ce anomalies, calculated from Ce/Ce^* ($Ce_{(SN)}/0.5Pr_{(SN)} + 0.5La_{(SN)}$) and Pr/Pr^* ($Pr_{(SN)}/0.5Ce_{(SN)} + 0.5Nd_{(SN)}$) values, were considered significant when Ce/Ce^* and Pr/Pr^* were less than and greater than 1, respectively (Bau and Dulski et al., 1996; Planavsky et al., 2010).

2.6.2 Sequential iron extraction redox analysis

Analysis was performed on three representative MFIF samples and the six sectioned bands of a typical NFIF sample using the method developed by Poulton and Canfield (2005) and data interpreted accordingly (e.g., Canfield and Poulton, 2005, 2011; Guilbaud et al. 2015; Sperling et al. 2015). Reagent blanks and geological standards were used for data calibration.

3 Results

3.1 Lithostratigraphy

Sedimentary structures, grain-size, lateral facies variations, vertical stacking trends, and key stratigraphic surfaces form the basis for facies analysis. Field-wide sedimentological and lithostratigraphical mapping of the CVSB in the summer and fall of 2014 enabled the assessment of the lateral and vertical coverage of the Milos iron oxide-rich facies relative to the Mn-rich sandstones that dominate the Early Quaternary sedimentary basin (Fig. 2). Six stratigraphic sections, representing marine siliciclastic lithofacies sequences, were investigated along a ~1 km SW-NE trending portion of the CVSB infill (Supplementary Figs 1-7). Sequence stratigraphy was conducted on outcrops and vertical shafts and tunnels left behind by previous Mn mining activity. Two of those sections; Section A located at 36°44'17.85''N, 24°21'17.72''E and Section B located at 36°44'35.11''N, 24°21'11.25''E, contain

286 stratigraphic units composed of layered, bedded, or laminated rocks that contain ≥ 15
287 % Fe, in which the Fe minerals are commonly interlayered with quartz or chert, in
288 agreement with the definition of BIFs (James, 1954; Gross, 1980; Bekker et al.,
289 2010). These IFs are descriptively referred to here as microfossiliferous iron
290 formation (MFIF) according to Chi Fru et al. (2013, 2015), and non-
291 microfossiliferous iron formation (NFIF) (this study), respectively (Fig. 2). The MFIF
292 and the NFIF occupy at most $\sim 20\%$ of the entire CVSB infill. The stratigraphy and
293 sedimentary lithofacies are illustrated below, using lithofacies codes modified after
294 Bouma (1962), Miall (1978, 1985), Lowe (1982), Mutti (1992) and Shanmugam
295 (2016).

296 Further field stratigraphic survey revealed considerable lithologic variability
297 within three fault-bounded volcanosedimentary sub-basins in the CVSB (Fig. 2),
298 which for the sake of simplicity are referred to as Basin 1—host of the MFIF; Basin
299 2—host of economic grade Mn ore; and Basin 3—host of the NFIF (Fig. 2). Each
300 section is framed by distinct marginal normal faults that strike in the NW-SE and NE-
301 SW to NNE-SSW directions, distinguishable by distinct lateral sedimentary facies
302 exhibiting unique vertical sequence stratigraphy (Fig. 2; Supplementary Figs 1-7).
303 Faulting in the CVSB is related to major geographical activation of extensional
304 structures at intervals that shaped Milos into a complex mosaic of neotectonic units
305 (Papanikolaou et al., 1990; van Hinsbergen et al., 2004).

306

307 **3.1.1 Section A ($36^{\circ}44'17.85''\text{N}$, $24^{\circ}21'17.72''\text{E}$)**

308 Informally known as “Little Vani”, Section A is the type section containing the MFIF
309 at the base. It crops out in the W-SW edge of the CVSB (Figs 1 & 2) as a $\sim 6\text{--}7$ m high

311 cliff resting stratigraphically on submarine dacitic and andesitic lavas and domes.

312 This section extends laterally in the N-NE direction for an estimated 300–500 m.

313 Lithologically, the MFIF comprises laminated and massive fine-grained red

314 and white weathered ferruginous jaspelitic red chert layers (Chi Fru et al., 2013,

315 2015). The chert layers contain morphologically distinct Fe minerals dispersed in a

316 fine-grained siliceous matrix (Fig. 3), marked by the notable absence of pyrite and an

317 low S content (Chi Fru et al., 2013, 2015). Layers are tabular and typically laterally

318 continuous at scales of several meters, whereas wave and current structures (e.g.,

319 cross-lamination) are generally absent from the MFIF. The hematite-rich MFIF

320 laminae (Table 1) are built by massive encrustation of anoxygenic photoferrotrophic-

321 like microbial biofilms by precipitated Fe (Chi Fru et al., 2013). The base of the MFIF

322 outcrop, is visibly mineralized by black diffused bands/veins composed of Mn oxides

323 (Fig. 4 & Table 1).

324 A markedly ferruginous 2-3 m-thick section immediately overlies the MFIF,

325 comprising a distinct package of Fe-rich beds that transition up the section (Figs 4A

326 & 5). The lower 1-2 m consist of fine-grained sandstone beds that are well to

327 moderately sorted, containing a 20-40 cm thick portion dominated by plane parallel-

328 laminated sandstone/sandy tuff, massive to plane parallel-laminated sandstone/sandy

329 tuff, and massive sandstone/sandy tuff lithofacies (Fig. 5; Supplementary Fig. 1). The

330 fabric of these Fe-rich sandstone facies consists of sub-angular to sub-rounded and

331 100–600 μm fine to medium-grained volcanoclastic K-feldspar grains, making up to

332 75% of the total rock, with variable amounts of quartz and clay mineral grains.

333 The latter are overlain by a ~1-1.5 m sequence of poorly-sorted tabular clast-

334 supported pebble-to-cobble conglomerate beds with an erosional base, grading

335 upward into coarse to medium-grained sandstone/sandy tuff beds, with alternating

Ernest Chi Fru 4/4/2018 23:13

Deleted: extremely

337 conglomerate cycles (Fig. 5), averaging 20-40 cm in thickness. The cobble/pebble
 338 conglomerate clasts include intraformational volcanic rocks (dacite, andesite),
 339 allochthonous volcanoclastic sandstone, and volcanoclastic microclasts (e.g. K-
 340 feldspar), cemented by hematite (Fig. 5; Chi Fru et al., 2013; Kiliyas et al., 2013a).
 341 Towards the westernmost edge of the “Little Vani” section, there is a facies change
 342 from the graded pebbly conglomerate/sandy tuff rhythms to a predominantly Fe-rich
 343 conglomerate bed (Fig. 6A), termed the conglomerate-hosted IF (CIF) in Chi Fru et
 344 al. (2015), with a maximum thickness of ~0.5 m and a cobble size range of ~10 cm.
 345 The Fe-rich conglomerate bed transitions upward into medium-grained pebbly reddish
 346 ferruginous sandstones with thin volcanic rock and sandstone pebble lenses. This, in
 347 turn, grades upwards into a very-fine-grained greenish glauconite-bearing plane
 348 parallel-laminated sandstone to siltstone bed; characterized by soft-sediment
 349 deformation structures, such as flame structures, convolute bedding and lamination
 350 structures, loop bedding, load casts, and pseudonodules (Supplementary Figs 1-2).
 351 The “Little Vani” section is eventually capped along an erosional surface by
 352 an overlying 1-2 m thick section dominated by medium to fine-grained and
 353 moderately to poorly-sorted reddish Fe-rich tabular sandstone beds, 10–40 cm thick,
 354 topped by patchy sub-cm to cm-thick Mn-rich sandstones (Fig. 5; Supplementary Figs
 355 1-2). Dominant lithofacies of the Fe-rich sandstone cap include planar and hummocky
 356 cross-bedding, exhibiting bioturbation in places. The Fe-rich lithofacies cap is
 357 laterally discontinuous, thinning out basinwards towards the N-NE, and can be
 358 observed smoothly grading into a 1-2 m thick section composed of cm to sub-cm-
 359 thick Mn-rich volcanoclastic sandstone lithofacies, described below in Section B. No
 360 Fe-rich hydrothermal feeder veins are obvious in the MFIF. However, feeder veins

and Mn horizons can be observed to truncate laminations in the MFIF, and up through the whole “Little Vani” section (e.g., Figs 4C & 5).

The MFIF rests directly on the submarine dacites-andesites that were deposited in a relatively shallow submarine environment (Stewart and McPhie, 2006). The fine-grained, finely laminated nature of the MFIF, and, the lack of evidence of current or wave structures (e.g., symmetric ripples or hummocky cross-stratification), coupled to the absence of volcanogenic detrital particles and intraclast breccia structures, indicate a low energy sedimentation environment, marked by negligible volcanic interference (e.g., Tice and Lowe, 2006; Konhauser et al., 2017). This interpretation is supported by the observed enrichment of Fe in the MFIF; a characteristic of relatively deeper water lithofacies (Konhauser et al., 2017). This view is compatible with the proposition that hematite enrichment in the MFIF was under the control of photoferrotrophic biofilms (Chi Fru et al., 2013) known to thrive at lower light intensities (Kappler et al., 2005; Li et al., 2013; Konhauser et al., 2017). The quiet environmental conditions would have ensured the formation of such stable photoferrotrophic biofilms over extended periods of time that would have facilitated the oxidation of hydrothermally released Fe(II) and the deposition of Fe(III) minerals.

In the overlying sandstone-conglomerate facies, the presence of sedimentary structures indicative of wave action and currents (e.g. cross-stratification), that signify rapid deposition during a high energy event, are consistent with a switch to a shallow-submarine high energy environment (Stewart and McPhie, 2006; Chi Fru et al., 2015). This shift in depositional environments may have been controlled by a combination of submarine volcano-constructional processes, synvolcanic rifting and volcano-tectonic uplift known to have formed the CVSB (Papanikolaou et al., 1990; Stewart and McPhie, 2006).

386

387 **3.2 Section B (36°44'35.11''N, 24°21'11.25''E)**

388 This ~8-10 m thick fault-bounded stratigraphic section, here referred to as
389 “Magnus Hill”, is the type section that contains the NFIF (Figs 2 & 7; Supplementary
390 Figs 3-4). Two lithostratigraphic units—a lower unit A and an upper unit B—are
391 identified in this study. Unit A is made up of a lower sandstone facies that is ~4-5 m
392 thick, dominated by a Mn-oxide cement, overlain by reddish brown Fe-rich massive
393 sandstone beds (Fig. 8 & Supplementary Figs 3-4). The lower sandstone facies
394 represents the host of the main economic grade Mn oxide ores in the CVSB. This
395 constitutes part of a separate study devoted to the Mn ores and will not be dealt with
396 further here. Unit B, ~5 m thick, unconformably overlies unit A and comprises two
397 distinct packages of beds that transition up section from brownish pebble
398 conglomerate layers (0.5-1.0 m thick), in contact with the very fine-grained NFIF
399 deposit (Supplementary Fig. 8 & 9). The NFIF is capped by patchy cm-thick
400 crustiform Mn oxides. Bifurcating feeder veins composed of barite, quartz and Mn-
401 Fe-oxide minerals cut through the underlying sandstone beds (Supplementary Fig. 4).

402 The NFIF is composed of banded Fe-rich rocks (Fig. 7) exposed on the topmost
403 part of “Magnus Hill”. About 2-3 m thick, the NFIF consists of mm to sub-mm thick,
404 dark grey and brown Fe-rich bands, interbanded with reddish brown Si-rich layers
405 (Figs 7 & 9-11; Supplementary Figs 10-11). Sedimentary structures in the NFIF are
406 predominantly characterized by rhythmic mm to sub-mm thick laminations (e.g., Fig.
407 7). The iron oxide-rich bands made up mainly of hematite (Table 1 & Fig. 10C) are
408 typically composed of very fine-grained angular to sub-angular volcanic dust material
409 (i.e., fine volcanic ash with particle size under 0.063 mm, K-feldspar, tridymite and
410 cristobalite (Table 1) in an amorphous Si and crystalline hematite matrix (Fig. 12)).

411 The predominantly amorphous Si-rich bands are typically planar, finely laminated and
412 composed of microcrystalline to cryptocrystalline ferruginous chert.

413 The NFIF is directly overlain by a ~1 m thick laminated to massive well-
414 indurated, nodular-pisolitic ironstone bed (Fig. 8A, C & D) that locally preserves a
415 sub-horizontal fabric reflecting the bedding in the original sediment or contain various
416 ferruginous clasts such as fragments, nodules, pisoliths, and oololiths set in a hematite-
417 rich siliceous matrix (Fig. 8C). Scattered cm scale pisoliths display a crude concentric
418 internal layering, characterized by open and vermiform voids filled by cauliflower-
419 like Mn oxides overprint (Fig. 8D). The ferruginous NFIF lithofacies are interpreted
420 to represent the deepest water deposits in the “Magnus Hill” section based on its very
421 fine-grained sedimentary composition, fine laminations and a paucity of intraclast
422 breccias. These, combined with the lack of evidence for wave and current-formed
423 sedimentary structures (e.g., hummocky cross-stratification, trough and ripple cross-
424 stratification), indicate quiet water low energy sedimentation, likely below wave base
425 (Simonson and Hassler, 1996; Trendall, 2002; Krapež et al., 2003; Konhauser et al.,
426 2017).

427 We interpret that each graded Fe oxide-rich band of the NFIF (Supplementary
428 Fig. 9), represents an individual fallout deposit from a proximal pyroclastic eruption.
429 This interpretation is supported by normal grading in fine volcanic ash content that
430 reflects their likely origin as pyroclastic fallout deposits in an otherwise quiet water
431 setting. For example, tridymite is a stable SiO₂ polymorph formed at low pressures of
432 up to 0.4 GPa and at temperatures of ~870-1470 °C (Swamy et al., 1994; Morris et al.,
433 2016). The coincidence of tridymite formation with silicic volcanism is in agreement
434 with the widespread distribution of andesite, dacite and rhyolite lava domes in the
435 CVSB. For example, vapour phase production of tridymite, together with sanidine

[mineralization](#) (Fig. 10), are principally associated with rhyolite ash flow (Breitkreuz, 2013; Galan et al., 2013). Similarly, Cristobalite is a SiO₂ polymorph [linked](#) with high temperature rhyolitic eruptions (Horwell et al., 2010). Finally, in situ carbonaceous laminations are absent, suggesting that benthic microbial mat growth had no influence on deposition of the NFIF. Ironstones overlying the NFIF are difficult to interpret with the existing data, but may represent supergene ferruginous duricrust formation resulting from subaerial weathering (Anand et al., 2002).

3.3 Geochemistry

3.3.1 Geochemistry of the individual Fe-rich and Si-rich bands

The SEM-EDS-electron micrographs of the NFIF thin sections reveal distinct Fe bands and Si-rich layers alternating periodically with each other in a fine sediment matrix as shown by the grain size (Figs 9 & 11 & Supplementary Figs 9-11). Laser ablation ICP-MS line analysis indicates Si and Fe count intensities in the Milos BIF-type rocks are comparable to the 2.5 Ga Precambrian BIF reference from the Kuruman IF formation, Transvaal Supergroup, South Africa (Fig. 11). The laser ablation ICP-MS data further show an inverse correlation between Fe and Si, the two major elemental components of BIFs, irrespective of the thousands of millions of years gap separating the Precambrian deposit from the recently formed Milos IF formation.

3.3.2 Mineralogy of the individual Fe-rich and Si-rich bands

No other Fe(III)(oxyhydr)oxide minerals have been identified in the Cape Vani Fe-rich facies different from hematite. Electron imaging of the NFIF Fe-rich bands suggests Si, Al and K-rich phases are mostly associated with the volcanoclastic

462 material predominated by K-feldspar clasts (Fig. 9; Supplementary Figs 10 & 11). A
463 unique feature of the NFIF is that the hematite in the Fe-rich bands occurs in tight
464 association with a carbonaceous material (Fig. 10C), but not for the hematite in the
465 Fe-rich sandstones and in the MFIF. This is also the case for the CIF overlying the
466 MFIF. Hematite showing a fluffy texture and at times presenting as framboidal
467 particles, is sprinkled in the Si-rich cement containing traces of Al and K in the MFIF
468 rocks (Fig. 3). Lack of association of the framboidal-iron-rich particles with S,
469 following SEM-EDS analysis, rules out a pyrite affiliation and is consistent with the
470 non-sulfidic depositional model suggested by the sequential iron extraction redox
471 proxy (Fig. 13D). TEM analysis suggests platy nano-Fe oxide-rich particles
472 predominate in the NFIF and MFIF, confirmed by overlaid X-ray Energy Dispersive
473 spectra taken from selected areas (Fig. 12) and consistent with the XRD data showing
474 hematite in both samples. The platy hematite needles in the Milos BIF-type rocks are
475 morphologically, and by size, comparable to hematite needles reported in the ~2.5 Ga
476 Kuruman BIFs (Sun et al., 2015).

477 Unlike the Fe-rich bands, volcanoclasts in the Si-rich bands are much smaller
478 in size, occurring mainly as fine-grained (Supplementary Fig. 8-11), signifying
479 predominant precipitation during periods of weakened hydrothermal activity. The
480 SiO₂ matrix in both the MFIF and NFIF are fine-grained, occurring mainly as
481 amorphous opal in the NFIF (Figs 10B & 12A-B), whereas in the MFIF it is mainly
482 present as crystalline quartz (Fig. 12C-D). Relative concentrations of Al, K and Ti in
483 the samples are generally low, with bulk-measured concentrations in both the Si-/Fe-
484 rich bands, together with the SiO₂ and Fe₂O₃ content, covarying with continental crust
485 concentrations (Fig. 13A). Mn impregnation of the MFIF, preserved in the form of
486 replacement layers mostly identified as cryptomelane [K(Mn⁴⁺,Mn²⁺)₈O₁₆] (Table 1),

is below detection in the NFIF. Rare hausmannite ($\text{Mn}^{2+}\text{Mn}^{3+}_2\text{O}_4$) was detected in a few cases in the MFIF (Fig. 10D).

3.3.3 Hydrothermal versus continental weathering

Trends of major elements from which CIA indices were calculated (Fig. 13B), covary with those of the continental crust (Fig. 13A). Continental crust averages, refer to the zone from the upper continental crust to the boundary with the mantle (Rudnick & Gao, 2003). The calculated CIA indices average 52 with one outlier at 22 (Fig. 13B). No distinct relationship could be established between the CIA indices and the respective IFs or between the distinct alternating Si- and Fe-rich bands (Fig. 13). Highly weathered clay minerals resulting from the chemical decomposition of volcanic rocks, e.g., kaolinite representing maximum CIA values of 100 or 75-90 for illite, are absent in the analyzed materials. The absence of carbonates in the rocks strengthened the CIA indices, since CIA indices are expected to be lower when Ca carbonates are present (Bahlburg and Dobrzinski, 2011). TiO_2 content, a detrital proxy, is mostly constant and covaries with the CIA values (Fig. 13B), suggesting little variability and limited continental weathering input. A fairly strong negative linear correlation was found between SiO_2 and Fe_2O_3 values normalized to TiO_2 (inset, Fig. 13B).

3.3.4 Redox reconstruction

Redox reconstruction by sequential iron extraction (Poulton and Canfield, 2005, 2011; Guilbaud et al., 2015; Sperling et al., 2015) is consistent with deposition of both the MFIF and NFIF facies beneath an anoxic, ferruginous bottom water body (Fig. 13C-D). The shale-normalized REE values ($\text{REE}_{(\text{SN})}$) for both the MFIF and

512 NFIF are consistent with previous reports (Chi Fru et al., 2013, 2015), showing
 513 patterns typical of marine sedimentary environments affected by hydrothermal
 514 activity throughout Earth's history (e.g., Planavsky et al., 2010). There is a notable
 515 absence of significant negative $Ce_{(SN)}$ anomalies for both the MFIF and NFIF (Fig.
 516 14A-B). These observations are statistically corroborated by true Ce anomalies.
 517 Further, the Eu/Eu* anomaly averages for the MFIF and NFIF and the distinct Fe-/Si-
 518 rich bands, suggest a $\sim 2\times$ higher Eu/Eu* signal for the Si-rich bands relative to the
 519 Fe-rich bands and between the MFIF and NFIF deposits (Fig. 14C). Average Pr and
 520 Yb shale-normalized ratios (Pr/Yb^*), a light vs. heavy REE enrichment proxy
 521 (Planavsky et al., 2010), indicate similar depleted levels of light and heavy REE in
 522 both the NFIF and MFIF, as well as in the Fe- and Si-rich bands (Fig. 14C). This
 523 independent verification of the anoxic depositional conditions using the sequential Fe
 524 proxy, suggests the NASC normalization protocol effectively captures the redox
 525 depositional conditions of the Milos IF.

526

527 **3.4 Lipid biomarker distribution and chemotaxonomy**

528 Bulk $\delta^{13}C_{org}$ averaged -25.4‰ (SD: ± 0.22); -25.2‰ (± 0.26) for NFIF Fe-/Si-rich
 529 bands and -25.6‰ (SD: ± 0.12) for bulk MFIF, respectively (Table 2). A fractionation
 530 effect between the alternating Fe-/Si-rich layers ($\Delta^{13}C_{Fe-rich\ NFIF-Si-rich\ NFIF}$) is estimated
 531 to be $\sim 0.23\text{‰}$ (SD: ± 0.036), while $\Delta^{13}C_{Fe-rich\ NFIF-MFIF}$ and $\Delta^{13}C_{Si-rich\ NFIF-bulk\ MFIF}$, is
 532 0.13‰ (SD: ± 0.11) and 0.36‰ (SD: ± 0.14), respectively. These differences are small
 533 and within the margin of error of analysis, suggesting no strong distinction in $\delta^{13}C_{org}$
 534 preserved in the different IFs and their various facies. They are interpreted to mean
 535 similar carbon fixation processes operated during intervals of predominant Si and
 536 Fe(III)(oxyhydr)oxides deposition in both IFs. Attempts to discriminate between these

environments by lipid biomarker analysis revealed mainly C₁₆-C₁₉ fatty acid methyl esters (FAME) in the Fe-rich NFIF bands and in bulk MFIF, while the Si-rich NFIF bands contain mainly C₁₂-C₂₁ FAMES, suggesting either selective preservation (lipid recovery was lower in the Fe-rich MFIF bands) or shifts to different potential biological populations during the deposition of the different layers. Preserved lipids discriminate against typical microbial lipid biomarkers like hopanoids, while C3 plant FAME are detected in all studied materials (Fig. 15). However, the anaerobic bacteria indicator, 10MeC_{16:0} FAME, was identified in a few bands.

4 Discussion

4.1 Sedimentological processes

The three sub-basin division of the CVSB is consistent with previous proposals suggesting that sedimentation within the CVSB was characterized by active synvolcanic rifting which must have been important in shaping basin topography and the creation of sub-basin architecture (Papanikolaou et al., 1990; Stewart and McPhie, 2006; Liakopoulos et al., 2001; Papavassiliou et al., 2017). Moreover, this tectonic regime would suggest that the location(s) of volcanism were continually changing relative to the two stratigraphic sections, which themselves were also being affected, i.e. changes in depositional water depth and sedimentation style or and/or that local submarine or subaerial topographic highs impeded the lateral continuity of sedimentary units (Stewart and McPhie, 2006). Chi Fru et al. (2015) have suggested there is an upward deepening of the overall depositional setting recorded in the “Little Vani” section, consistent with rifting during CVSB infilling time.

The CVSB floored by dacitic/andesitic lava domes and overlain by volcanoclastic infill, dates back to Upper Pliocene-Lower Pleistocene. A complex

562 mosaic of lithologically diverse sedimentary units (blocks), confined by neotectonic
563 marginal faults, characterizes the CVSB (Fig. 2). The most pronounced of these faults
564 being the NW-trending Vromolimni-Kondaros fault (Papanikolaou et al., 1990) that
565 has been proposed as the trigger of the hydrothermal activity that deposited Mn ore in
566 the CVSB (Papanikolaou et al., 1990; Liakopoulos et al., 2001; Alfieris et al., 2013;
567 Papavassiliou et al., 2017). The stratigraphically tight coupling between Mn and Fe
568 deposition, linked by Fe oxide minerals in feeder-veins, and positive Eu anomalies
569 (Fig. 14) indicating vent-sourced Fe (Maynard, 2010), associate Fe mineralization to
570 fault-triggered hydrothermalism in the CVSB. This is consistent with models of
571 geothermal fluid circulation along fault lines as conduits for the Mn-rich fluids that
572 formed the Milos Mn ore deposit (Hein et al., 2000; Liakopoulos et al., 2001; Glasby
573 et al., 2005; Kiliyas, 2011; Papavassiliou et al., 2017). More importantly, the overall
574 complex neotectonic structure of the CVSB (Papanikolaou et al., 1990) would explain
575 the creation of restricted basins, with sedimentological, lithological and geothermal
576 conditions that enabled the development of unique biogeochemical circumstances in
577 which the NFIF and MFIF formed.

578 The presence of the three depositional basins is supported by the fact that the
579 sequence lithologies in each fault-bound unit are characterized exclusively by
580 occurrences of specific and variably thick stratigraphic packages that tend to be
581 absent in others. For example, the MFIF occurs restricted to basin 1 and the NFIF to
582 Basin 3. Basin 2 is further distinguished by 35-50 m thick interbedded ore-grade Mn-
583 mineralized and glauconitic sandstones/sandy tuffs, much less developed in Basins 1
584 and 3 (Fig. 2). The presence or absence of a stratigraphic sequence, together with its
585 thickness variation, are interpreted as a result of local syntectonic sediment formation
586 conditions in each basin as a result of block tectonic movements along fault lines

587 (Papanikolaou et al., 1990). It may also be attributed to unique basin scale water
588 column redox conditions (e.g. Bekker et al., 2010, and references therein), post-
589 depositional erosion and changing sea level stand (Cattaneo & Steel, 2000).

590 The lack of hydrothermal feeder veins or seafloor exhalative structures (i.e.,
591 chimneys) in the MFIF and NFIF lithologies, suggests that hydrothermal Fe(II) was
592 delivered by diffuse flow and that the Milos-IF formed on the seafloor.
593 Further, mineralisation of the MFIF is suggested to have occurred during two major
594 hydrothermal venting stages. The first produced the MFIF and the second
595 contaminated it with cryptomelane. Cryptomelane in the MFIF is therefore not a
596 replacement product of primary Mn oxides formed during the deposition of the MFIF,
597 because the anoxia prevailing in Basin 1 at the time (Figs 2 & 13C) would have
598 precluded the precipitation of Mn oxide minerals, hinting that a second phase
599 hydrothermal fluid emission rich in dissolved Mn, directly precipitated cryptomelane
600 from solution as a secondary mineral relative to the primary Fe(III)(oxyhydr)oxides in
601 the MFIF. This occurred during an episode when the MFIF deposit must have been
602 exposed to oxygenated fluids, most likely through mixing with seawater at depth,
603 indicated by the abundance of cryptomelane at the base of the MFIF. Our model for
604 cryptomelane precipitation in the MFIF is therefore different from the one suggesting
605 diagenetic transformation of primary Mn ores at Milos (Hein et al., 2001;
606 Liakopoulos et al., 2001; Papavassiliou et al. 2017).

607 Geomorphological/chemical reconfiguration orchestrated the deposition of the
608 NFIF in a deeper, small-restricted basin (Fig. 2). The deepening of Basin 3 is reflected
609 in the underlying graded conglomerate bed that exhibits an upward fining trend,
610 followed by transition into the fine-grain NFIF. The conglomerate bed may represent
611 rapid deposition during a high-energy event, i.e. storm or mass flow, whereas the

612 upward fining in the bed is better explained by the depositional mechanism losing
613 energy through time. These high-energy conditions must have ceased during the
614 deposition of the overlying NFIF, where we interpret that increased abundance of
615 finely laminated IF and decreased evidence of storm and/or mass flow reworking
616 reflects deepening conditions. The hypothesized deepening of Basin 3 is consistent
617 with the interpretation that active rifting was an important mechanism in the
618 formation of the CVSB (Papanikolaou et al., 1990).

619

620 **4.2 Formation Mechanism of The Milos BIFs**

621 **4.2.1 Paragenetic sequence**

622 It is stressed that the previously generalized model proposed for biological deposition
623 of the Milos IF, refers exclusively to parts of what is [here](#) designated as MFIF (Chi
624 Fru et al., 2013). The NFIF is banded, but does not display the typical microfossils
625 seen in the MFIF, where diffused microbanding apparently relates to the distribution
626 of microbial mats in thin sections (Chi Fru et al., 2013, 2015). The distinction of
627 microcrystalline quartz and amorphous silica phases in the MFIF and NFIF,
628 respectively, together with nano-crystalline hematite particles, suggests a primary
629 amorphous silica origin in both deposits, diagenetically transformed to quartz in the
630 MFIF. The difference in silica crystallinity between the IFs is concurrent with the
631 older age predicted for the MFIF relative to the NFIF, from reconstructed sequence
632 stratigraphy (Fig. 2). Hematite in BIFs is generally interpreted, based on
633 thermodynamic stability, to be a transformation product of various primary Fe(III)
634 minerals, with ferrihydrite often proposed as the primary water column precipitate
635 (Glasby and Schulz, 1999; Bekker et al., 2010; Johnson et al., 2008; Percoits et al.,
636 2009). It is thought that acidic pH yields mainly goethite while hematite is produced

Ernest Chi Fru 9/4/2018 10:10

Deleted: now

638 at circumneutral pH (Schwertmann and Murad, 2007). The notable absence of
639 diagenetic magnetite and Fe carbonates (siderite and ankerite), point to negligible
640 coupling of primary Fe(III) oxyhydroxides reduction to organic matter oxidation by
641 the dissimilatory iron-reducing bacteria during burial diagenesis (Johnson et al.,
642 2008). Minor occurrence of iron-silicate phases (Chi Fru et al., 2015) indicates an
643 origin of the hematite precursor in seawater independent of the iron silicate proposed
644 in some cases (Fischer and Knoll, 2009; Rasmussen et al., 2013, 2014). The up to 50
645 wt% Fe content recorded in the Fe-rich bands, indicate that large amounts of
646 dissolved Fe(II) was intermittently sourced and deposited as primary Fe(III) minerals,
647 through various oxidative processes in the depositional basin.

648 Importantly, the CIA analysis does not support mass weathering and
649 mineralization of terrestrial Fe and Si, in agreement with the absence of rivers
650 draining into the CVSB (Chi Fru et al., 2013). The specific identification of plant
651 biolipids would at face value imply post-depositional contamination. However,
652 samples were sawn to remove exposed layers and only the laminated bands for the
653 NFIF were analyzed. Modern sediments from Spathi bay, located Southeast of Milos
654 Island where hydrothermal activity is presently [occurring](#) at 12.5 m below sea level,
655 revealed similar plant lipids as recorded in the Quaternary IF (Fig. 15G). Post-
656 depositional contamination with terrestrial plant lipids is therefore ruled out for the
657 idea that recalcitrant plant biomass probably entered the sediments via seawater
658 entrainment at the time of deposition (see Naden et al., 2005). This finding
659 necessitates the careful interpretation of bulk $\delta^{13}\text{C}_{\text{org}}$ values obtained from both the
660 modern and ancient Milos sediments, involving in situ and ex situ biological
661 contributions to $^{13}\text{C}_{\text{org}}$ fractionation by various known carbon fixation pathways
662 (Preuß et al., 1989; Berg et al., 2010).

663

664 4.2.2 Tectono-sedimentary processes and band formation

665 Fluctuation in hydrothermal activity is proposed to account for the banding in the
666 NFIF (Fig. 16), under redox depositional conditions inferred to be mainly reducing
667 for both investigated IFs, consistent with previous reports (Chi Fru et al., 2013, 2015).
668 Positive Eu anomalies indicate a hydrothermal origin for all but one of the sample
669 suite (Fig. 14A). However, statistically calculated Eu/Eu^* anomalies ($Eu_{(SN)}/$
670 $(0.66Sm_{(SN)} + 0.33Tb_{(SN)})$) to correct for differences in Gd anomalies commonly
671 encountered in seawater (Planavsky et al., 2010) are in the range of 0.1-0.58,
672 averaging 0.42. The lack of statistically significant true negative Ce anomalies (Fig.
673 14B) supported by sequential Fe redox reconstruction (Fig. 3C-D; Planavsky et al.,
674 2010; Poulton and Canfield, 2005, 2011; Guilbaud et al., 2015; Sperling et al. 2015),
675 indicate a reducing depositional environment for both The MFIF and the NFIF.

676 CIA analyses traditionally provide relative information on contributions from
677 chemical weathering to sediment deposition, linked to operative hydrological and
678 climatological patterns on land. This information is often gleaned from ancient and
679 modern soils and from reworked siliclastic deposits in marine basins (Maynard, 1993;
680 Bahlburg & Dobrzinski, 2011). The calculated CIA values, however, are closer to the
681 range obtained for unweathered and or only minimally weathered volcanic rocks (e.g.,
682 Nesbitt & Young, 1982; Bahlburg & Dobrzinski, 2011), thus pointing to a
683 predominantly volcanic and/or hydrothermal provenance for the clastic sedimentary
684 materials in the IFs.

685 It has been suggested that the release of reduced submarine hydrothermal fluids
686 contributed towards maintaining water column anoxia during the deposition of
687 Precambrian BIFs (Bekker et al., 2010). The calculated Eu anomalies (Fig. 14) and

petrographic data showing volcanoclastic detritus (i.e., K-feldspar, sanidine, tridymite, cristobalite) as key rock components are in agreement with a submarine hydrothermal source for the investigated IFs. The coarse volcanoclastic detritus embedded in the Fe-rich bands compared to the finer particles in the Si-rich layers, highlights rapid oxidation of Fe(II) that coincided with periodic cycles of hydrothermal/volcanic discharge of new materials into the water column. However, the fine-grained nature of both the MFIF and NFIF deposits suggests that deposition likely occurred away from where such activity was occurring or that volcanic/hydrothermal discharge of Fe and Si was non-eruptive and disruptive. The Fe-rich bands repetitively revealed hematite grains cementing the denser volcanoclastic fragments that gradually diminish upwards into a zone of fine-grained hematite before transitioning into Si-rich bands consisting mainly of finer volcanoclastic detritus. These observations provide three valuable interpretational considerations for proposing a model for the formation of the alternating Si and Fe-rich bands.

1. The Si and Fe oxides-rich bands are primary precipitates formed in the water column, by a process in which the precipitation of amorphous Si occurred during quiescent non-volcanic intervals, with the oxidation and precipitation of reduced Fe intermittently introduced into the water column by volcanic/hydrothermal activity to form the Fe oxides.
2. The repetitive zonation of distinct particle sizes, suggests density gradient sedimentation that requires a water column-like environment, rather than diagenetic alteration of pre-formed sediments by hydrothermal fluids.
3. The reducing depositional conditions do not support sediment diagenesis as an alternative model for explaining the origin of the Milos IF. This is because the oxidation of ferrous Fe supplied in reduced hydrothermal fluids, must

713 interact with a sizeable pool of oxygen, enabling microaerophilic bacterial
714 oxidation of ferrous iron to Fe(III)(oxyhydr)oxides (Johnson et al., 2008; Chi
715 Fru et al., 2012). Otherwise, light-controlled photoferrotrophy oxidizes
716 ferrous Fe to form ferric (oxyhydr)oxides in the absence of oxygen in the
717 photic zone of the water column (Weber et al., 2006).

719 4.2.3 Biological involvement

720 Hematite precipitation in the MFIF on microbial filaments (Chi Fru et al., 2013) was
721 previously used to propose a generalized basin-scale mechanism for the deposition of
722 Fe-rich rocks in Cape Vani. However, such filaments are absent in the NFIF, while
723 pure hematite grains are tightly bound to relics of an organic matter signal carrying a
724 maximum $\delta^{13}\text{C}_{\text{org}}$ signature of -25‰ (Table 2). Similar processes are recorded in
725 modern marine sediments where interactions between Fe and free organic matter has
726 been reported to enable the preservation up to 21.5wt% of total organic carbon over
727 geological time scales (Lalonde et al., 2012). Moreover, Fe generally traps and
728 preserves organic matter at redox interfaces (Riedel et al., 2013). The data appear to
729 suggest that the mechanism of Fe(III) (oxyhydr)oxide precipitation and preservation
730 varied between the two IFs. The photoferrotrophic-like filamentous fossils reported in
731 the MFIF (Chi Fru et al., 2013), are absent in the NFIF. This does not, however, rule
732 out the potential role of microbial involvement in Fe(II) oxidation, as diverse
733 microbial taxa carry out this process, several of which are non-filamentous (Chi Fru et
734 al., 2012). However, our data is insufficient to enable clear quantification of the levels
735 of abiotic vs. biotic contribution to Fe(II) oxidation in the NFIF. Nevertheless, the
736 inferred predominantly anoxic depositional conditions as explained above, together
737 with the identification of anaerobic bacteria biomarkers in the laminated bands,

Ernest Chi Fru 4/4/2018 23:14

Deleted: ,

Ernest Chi Fru 4/4/2018 23:16

Deleted: an extremely rare sediment characteristic, precipitates

Ernest Chi Fru 4/4/2018 23:15

Deleted:

Ernest Chi Fru 4/4/2018 23:16

Deleted: sunlight environments

743 intuitively favor significant contribution of anaerobic biological Fe(II) oxidation in
744 the precipitation of primary Fe(III)(oxyhydr)oxides in the NFIF. See Weber et al.,
745 2006, for a review of potential biological pathways to anaerobic Fe(II) oxidation.

746 Briefly, anaerobic microbial Fe(II) oxidation can proceed via nitrate reduction
747 and by photoferrotrophy to deposit Fe(III)(oxyhydr)oxides. These mechanisms have
748 been linked to microbial contribution to BIF formation (Weber et al., 2006; Kappler et
749 al., 2005) and also for the MFIF (Chi Fru et al., 2013). However, it is also possible
750 that microaerophilic neutrophilic Fe(II)-oxidizing bacteria likely played an important
751 role, assuming a depositional setting analogous to the Santorini caldera and Kolumbo
752 shallow submarine volcanoes, where such low-O₂-dependent microbial Fe(II)
753 oxidation has been identified to actively precipitate Fe(III)(oxyhydr)oxides (Kiliass et
754 al., 2013b; Camilli et al., 2015). It appears that in the MFIF, precipitating
755 Fe(III)(oxyhydr)oxide minerals were bound and preserved free of organic carbon or
756 that such organic carbon was diagenetically degraded. As was previously shown,
757 Fe(III)(oxyhydr)oxides completely replaced the organic content of the filamentous
758 microfossils in the MFIF (Chi Fru et al., 2013).

759 The 10MeC_{16:0} FAME identified in the rocks has been reported in anaerobic
760 organisms coupling nitrite reduction to methane oxidation (Kool et al., 2012), in
761 sulfate and iron-reducing bacterial species such as *Desulfobacter*, *Desulfobacula*
762 (*Bühning* et al., 2005; Dowling et al., 1986; Taylor and Parkes, 1983), *Geobacter*,
763 *Marinobacter* and the marine denitrifier, *Pseudomonas nautical* (Kool et al., 2006;
764 *Bühning* et al., 2005; Dowling et al., 1986). It had previously been proposed that post-
765 depositional denitrification was a potential pathway for early organic matter removal,
766 justified by the low rock organic carbon and nitrogen content in the Milos BIF-type
767 rocks (Chi Fru et al., 2013, 2015; Table 2). Equally, the detected 10MeC_{16:0} FAME

768 has also been found in anaerobic oxidation of methane (AOM) communities (Alain et
769 al., 2006; Blumenberg et al., 2004), originating from sulfate reducing bacteria.
770 However, bulk sediment $\delta^{13}\text{C}_{\text{org}}$ of -20‰ does not reflect AOM activity that is
771 expected to produce bulk $\delta^{13}\text{C}_{\text{org}}$ values that are $\leq -30\text{‰}$. Low $10\text{MeC}_{16:0}$ FAME
772 concentrations frustrated attempts at acquiring its compound specific isotopic
773 signature to enable further biomolecular level reconstruction of active microbial
774 metabolisms to explain Fe deposition mechanisms.

775 It is nevertheless puzzling why potential microbial biomarkers typical of marine
776 or hydrothermal vent environments are hardly preserved in the rocks, given that
777 microfossil evidence indicates a vast community of diverse prokaryotic assemblages
778 in the adjacent MFIF (Chi Fru et al., 2013, 2015). Moreover, sediments of the modern
779 Milos hydrothermal system and elsewhere on the HVA, are ubiquitously colonized by
780 microbial life, characterized by the marked large-scale absence or low abundance of
781 higher life forms, including plants (Kiliyas et al., 2013b; Camilli et al., 2015; Oulas et
782 al., 2015). One possibility could be the discriminatory preservation of lipids related to
783 their selectivity and reactivity towards Fe(III)(oxyhydr)oxides and clays or different
784 pathways to diagenetic degradation (e.g., Canuel & Martens, 1996; Lü et al., 2010;
785 Riedel et al., 2013). As noted, the carbonaceous materials in the BIF-type NFIF rocks
786 occur in tight association with hematite.

787 Importantly, prokaryotic biomarkers are suggested to poorly preserve in these
788 young BIF analogs. This raises the possibility that this may provide an important
789 explanation for why lipid biomarkers are yet to be extracted from Precambrian BIFs.
790 Moreover, the data are compatible with the low C_{org} recorded in BIFs of all ages,
791 suggesting that the low C_{org} abundance may not be due to metamorphism as often
792 proposed (Bekker et al., 2010) or to C_{org} oxidation by dissimilatory iron reducing

bacteria to form ^{13}C -depleted siderite and ankerite during diagenesis (Johnson et al., 2008; Bekker et al., 2010). The Milos BIF-type rocks are unmetamorphosed and lack iron carbonate, yet have vanishingly low C_{org} levels similar to the ancient metamorphosed BIFs. However, an alternative possibility is that the iron oxides may have been reduced through biological oxidation of organic carbon, but carbonate saturation was not reached (Smith et al., 2013).

4.2.4 Mn layers and the deposition of the Si-Fe-rich facies

Cryptomelane $[\text{K}(\text{Mn}^{4+}, \text{Mn}^{2+})_8\text{O}_{16}]$, which commonly occurs in oxidized Mn deposits resulting from mineral replacement and as open space fillings (Papavassiliou et al., 2016), is also common in the MFIF. This supports the idea of post-depositional impregnation of the base of the MFIF by Mn-rich fluids. Microscopic analysis supports the epigenetic origin of the Mn in the MFIF by revealing Mn oxides growing along fractures, impregnating and replacing Fe minerals (Fig. 4B-F). The macroscopically evident thinning out to disappearance of such Mn-rich horizons up the MFIF, coupled by their development along microfractures emphasizes this epigenetic origin. Mn is not a common feature of the NFIF, even though it sits on top of a thin sandstone layer that is highly mineralized with Mn, locally forming the cap of the main Mn ore at Cape Vani. The generally accepted view is that Mn-rich hydrothermal fluids rose and mineralized the Cape Vani sandstones (Hein et al., 2000; Liakopoulos et al., 2001; Glasby et al., 2005). Based on the stratigraphic location of the MFIF, which pre-dates the Mn-rich sandstones, it is proposed that impregnation of the MFIF by Mn was coeval with large-scale Mn ore mineralization of the Cape Vani sandstones, implying the entire basin was likely oxygenated at the time. The lack of Ce anomalies, confirmed by the sequential Fe extraction proxy data, suggests that

818 both the MFIF and the NFIF formed in anoxic settings. Similar data for the Mn oxides
819 have suggested formation in oxic settings (Glasby et al., 2005; Chi Fru et al., 2015).
820 This implies that Mn epigenetically replaced the MFIF, either because the basin was
821 tectonically uplifted into a high-energy oxygenated shallow water setting or that sea
822 level dropped, leading to partial metasomatism of the base of MFIF, when oxygenated
823 seawater mixed with reduced hydrothermal fluids and precipitated Mn. The lack of
824 significant Ce anomalies in the dataset, combined with the inferred deepening of basin
825 3 and the anoxic depositional conditions suggested by the sequential iron redox proxy,
826 further indicate that for the final deposition of the NFIF, an eventual deepening event
827 must have been triggered, resulting in deoxygenation of parts of the CVSB.

828 All of this is feasible with the three-basin-fault-bounded hypothesis as a
829 requirement for movement along fault lines in response to temporal tectonic
830 activation. The upward sequence transition from the Mn-rich sandstone facies,
831 through the pebbly conglomerate and the final termination in the overlying mud-
832 grained NFIF (Fig. 8B), reflect sedimentary features formed during multiple changes
833 in seawater levels (Cattaneo & Steel, 2000).

834 Uplifting is suggested by potential weathering of the NFIF to form the
835 ferruginous duricrust cap. Comparable ferruginous layers on Precambrian BIFs are
836 linked to pervasive subaerial chemical weathering, via the dissolution of the silica-
837 rich layers and precipitation of relatively stable Fe oxides in the spaces between more
838 resistant hematite crystals (e.g., Dorr, 1964; Shuster et al., 2012; Levett et al., 2016).
839 This collective evidence supports the existence of a geodynamic tectonic system
840 capable of producing shallow oxic to deeper anoxic basin conditions at different times
841 that would explain the existence of Mn and Fe oxide layers within the same
842 sedimentary sequence. For example, it is common knowledge that both Fe and Mn

843 oxides will precipitate in the presence of oxygen (Roy, 1997, 2006), with kinetic rates
844 usually being faster for the oxidation of reduced Fe than reduced Mn. In the Fe(II)-
845 rich conditions that prevail in anoxic settings, abiotic reactions between Fe(II) and Mn
846 oxides, produce Fe(III) leading to the dissolution of the Mn oxides to form reduced
847 Mn, implying Mn oxides should not accumulate (Dieke, 1985). Moreover, under these
848 conditions, biological precipitation of Fe(III) can occur rapidly, leaving dissolved Mn
849 in solution to be deposited when oxygen becomes available. Given that the
850 hydrothermal fluids of the Hellenic Volcanic Arc are commonly enriched in both
851 reduced Fe and Mn, the deposition of the MFIF and NFIF therefore implies there was
852 an existing mechanism that enabled the kinetic discrimination and deposition of the
853 oxides of Fe and Mn into separate settings, most likely dependent on prevailing redox
854 conditions. The accumulation of the ferruginous duricrust layer, overprinted by redox
855 sensitive Mn-nodules, above the NFIF indicates a new shallowing event might have
856 terminated the formation of the NFIF.

857

858 4.2.5 Modern analogs on the HVA

859 Mechanistic explanation for the development of potential stratified waters and
860 reducing conditions during the deposition of the Milos BIF is problematic. However,
861 evidence is available from present shallow submarine hydrothermal analogs in the
862 central part of the HVA, to which the CVSB belongs. These include:

863 (1) The crater floor of the Kolumbo shallow-submarine volcano (~600×1200
864 m), which rises 504 m from the crater floor to 18 m below sea level (Sigurdsson et al.,
865 2006; Kiliass et al., 2013b).

Ernest Chi Fru 5/4/2018 04:42

Deleted: from

Ernest Chi Fru 5/4/2018 04:43

Deleted: , near Santorini

868 (2) The N part of Santorini's submerged caldera walls, which rises from 390 m
869 below sea level to over 300 m above sea level (Druitt et al., 1999; Friedrich et al.,
870 2006; Nomikou et al., 2013; Camilli et al., 2015).

871 (3) The coastal embayments at the Kameni emergent volcanic islands in the
872 center of the Santorini caldera (Hanert, 2002; Nomikou et al., 2014; Robbins et al.,
873 2016).

874 The benthic waters within Kolumbo's crater potentially sustain O₂ depleted
875 conditions via stable CO₂-induced water column densification, and accumulation of
876 acidic water (pH ~5), extending ~10 m above the CO₂ venting crater floor (Kilias et
877 al., 2013b). This phenomenon is believed to lead not only to obstruction of vertical
878 mixing of bottom acidic water, but also to O₂ deprivation by precluding efficient
879 transfer of oxygenated surface seawater into the deeper crater layer. In addition,
880 diffuse CO₂ degassing is believed to be linked to the formation of Fe microbial mats
881 and amorphous Fe(III) oxyhydroxides on the entire Kolumbo crater floor (Kilias et
882 al., 2013b) and on the shores of Milos Island (Callac et al., 2017). Prerequisites for
883 the O₂-depleted conditions to happen are the closed geometry of the Kolumbo crater
884 and the virtually pure CO₂ composition of the released hydrothermal vent fluids that
885 produce O₂ stratification along a stable CO₂-pH gradient.

886 A similar scenario is reported for the Santorini caldera, where large (~5 m
887 diameter) CO₂-rich, acidic (pH, ~5.93) hydrothermal seafloor pools and flow
888 channels, develop within m-thick microbial Fe-mats on the seafloor slope at 250-230
889 m below sea level. Persistent hypoxia exists in these pools, representing concentrated
890 seafloor CO₂ accumulation centers generated by hydrothermal venting (Camilli et al.,
891 2015). Here, the dissolved O₂ content (~80 µM or less) in the pools is ~40 % depleted
892 relative to the surrounding ambient seawater (Camilli et al., 2015). These hypoxic

Ernest Chi Fru 5/4/2018 04:44

Deleted: re

894 conditions are comparable to or even lower than those measured in the CO₂-rich
895 oxygen minimum zones of coastal oceans, relative to seawater existing in equilibrium
896 with atmospheric pO₂ and pCO₂ pressures (Paulmier et al., 2008, 2011; Franco et al.,
897 2014). These conditions enable strong redox stratification of the pool waters, in which
898 unique Si- and Fe-rich microbial mats are associated with amorphous opal and
899 Fe(III)(oxyhydro)xides (Camilli et al., 2015). Importantly, the Fe microbial mats in
900 these CO₂-rich hypoxic pools are affiliated with specific microaerophilic Fe(II)-
901 oxidizing bacteria that accumulate Fe(III) oxyhydroxides (Camilli et al., 2015; Oulas
902 et al., 2015). These Fe bacteria are implicated in the deposition of the Precambrian
903 BIFs (Konhasuer et al., 2002; Planavsky et al., 2009; Bekker et al., 2010).

904 Hypoxia is also associated with the water column of the Fe(III)-rich coastal
905 embayments and their hydrothermal vents (≤ 1.0 m water depth), Kameni islands
906 (Hanert, 2002; Robbins et al., 2016 and references therein). Venting fluids are warm
907 (20-40 °C), acidic to circumneutral (pH 5.5-6.9), enriched in CO₂, Fe and Si
908 (Georgalas & Liatsikas, 1936, Boström et al., 1990; Handley et al., 2010; Robbins et
909 al., 2016). Water column stratification is expressed as decreasing O₂ with depth that is
910 positively related to Fe(III)(oxyhydr)oxide density and microaerophilic Fe(II)-
911 oxidizing bacterial prevalence (Hanert, 2002). Robbins et al. (2016) found that
912 Fe(III)-rich suspended particulate material in these “Fe bays” may be associated with
913 anoxia, extending up to the air-seawater interface, near the hydrothermal vents
914 (Hanert, 2002). They consist of ferrihydrite, goethite and microaerophilic Fe(II)
915 oxidizers.

916 However, the biogeochemical occurrence of these phenomena within the
917 localized confines of the Santorini caldera and Kolumbo crater, may however be
918 difficult to achieve in ordinary shallow submarine hydrothermal settings, such as

919 those occurring on the coast of present day Milos. The same may be true for Tatum
 920 Bay, where non-volcanic and unconfined diffuse hydrothermalism is widespread
 921 (Dando et al., 1996; Pichler & Dix, 1996; Pichler & Veizer, 1999; Stüben et al., 1999;
 922 Rancourt et al., 2001; Varnavas et al., 2005).

923 In the Kolumbo and Santorini hydrothermal fields, benthic pH averages 5.5 and
 924 the deposition of carbonates is markedly absent (Kiliyas et al., 2013b, Camilli et al.,
 925 2015; Robins et al., 2016). This conforms to observations in the MFIF and NFIF units
 926 where carbonate mineralization is not detected, thereby suggesting a similar low pH
 927 depositional environment for both the MFIF and NFIF. Ubiquitous
 928 Fe(III)(oxyhydr)oxide precipitation and enriched Si content are prevalent in the CO₂-
 929 rich-hypoxic shallow submarine Santorini caldera slope pools and the Kameni Fe-
 930 embayments where sulfide precipitation is restricted (Camilli et al., 2015; Robbins et
 931 al., 2016). Such sulfide-poor conditions are critical for the formation of BIFs (Bekker
 932 et al., 2010).

933 A high Si and Fe(III)(oxyhydr)oxide content, absence of detectable carbonate
 934 and Fe sulfide minerals, are hallmark characteristics of the Milos IF (Chi Fru et al.,
 935 2013, 2015; Fig. 13C-D). This depositional situation is different, for example, from
 936 the unconfined shallow submarine hydrothermal activity in Tatum Bay and Bahia
 937 Concepcion, Baja California Sur state, Mexico, where authigenic carbonate
 938 deposition is widespread (Canet et al., 2005; Pichler & Veizer, 1996, 2005).
 939 Moreover, there is strong geological evidence that within volcanic crater
 940 environments associated with high CO₂ emission, long-term water column redox
 941 stratification is possible under these special conditions. For example, Lake Nyos, a
 942 205 m deep volcanic crater lake, in Cameroon, Central-West Africa, undergoes CO₂-
 943 induced water column stratification, lasting several decades. The reducing bottom

Ernest Chi Fru 4/4/2018 23:19

Deleted: inhibited

Ernest Chi Fru 4/4/2018 23:19

Deleted: , or extremely rare (Robbins et al., 2016)

Ernest Chi Fru 5/4/2018 03:27

Deleted: -

Ernest Chi Fru 5/4/2018 03:27

Deleted: mineralization

Ernest Chi Fru 5/4/2018 03:39

Deleted: , coupled to a generally low S content

Ernest Chi Fru 5/4/2018 03:23

Deleted: have also been demonstrated for

Ernest Chi Fru 5/4/2018 03:23

Deleted: CVSB Fe formations

Ernest Chi Fru 5/4/2018 03:24

Deleted:)

Ernest Chi Fru 5/4/2018 03:41

Deleted: systems

Ernest Chi Fru 5/4/2018 03:51

Deleted: Further evidence is found in

Ernest Chi Fru 5/4/2018 03:43

Deleted:

Ernest Chi Fru 5/4/2018 03:46

Moved down [1]: (Ozawa et al., 2016; Kling et al., 2005)

Ernest Chi Fru 5/4/2018 03:43

Deleted: s

Ernest Chi Fru 5/4/2018 03:43

Deleted: (for example the shallow 205 m deep lake Nyos

Ernest Chi Fru 5/4/2018 04:36

Deleted: experiences—

Ernest Chi Fru 5/4/2018 03:47

Deleted: renowned as one of Earth's three CO₂ saturated volcanic lakes (Ozawa et al., 2016; Kling et al., 2005). Here

Ernest Chi Fru 5/4/2018 04:32

Deleted: is associated with

Ernest Chi Fru 5/4/2018 03:33

Deleted: bottom

968 | ~~waters contain~~ low sulfate and ~~elevated reduced Fe concentration~~ relative to the
 969 | ~~oxidized surface water~~ (Kling et al., 2005; Tiodjio et al., 2014; Ozawa et al., 2016).

971 5 Concluding remarks

972 This study shows the following new insights in light of what was previously known:

973 1. At least two distinct IFs (MFIF and NFIF) formed from hydrothermal mud,
 974 within two localized sub-basins in the ~1 km-long CVSB, ~2.66-1.0 Myr ago,
 975 controlled by local tectonism.

976 2. Local conditions of elevated and cyclic supply of ferrous Fe and dissolved Si,
 977 accompanied by ~~bottom water anoxic conditions~~ in a localized reservoir
 978 cutoff from the open ocean, can in principle allow the deposition of BIF-type
 979 rocks in a modern marine setting. The rarity of ~~this~~ type of ~~deposit~~, however
 980 suggests that ~~the~~ conditions ~~required for formation~~ are ~~not a frequent~~
 981 ~~occurrence~~ under the ~~present-day~~ oxygen-rich atmosphere.

982 3. A working model that band formation may involve potential
 983 Fe(III)(oxyhydr)oxide infilling of sediment pores and fractures during
 984 diagenesis, is not supported by the data. In addition to the lack of observation
 985 of such phenomena, as ~~shown~~ for replacive Mn mineralization, calculated Ce
 986 and Eu anomalies, together with sequential iron extraction analysis, are
 987 suggestive of anoxic depositional conditions likely induced by the release of
 988 reduced hydrothermal/volcanic fluids into a cutoff sedimentary basin.

989 4. ~~Both~~ Fe(III)(oxyhydr)oxides and Mn oxides ~~are precipitated in the presence~~
 990 ~~of oxygen~~. In ~~its~~ absence, ~~the formation of Mn oxides is inhibited~~, while
 991 ~~photoferrotrophy in the anoxic photic zone of redox-stratified waters oxidizes~~
 992 ~~reduced Fe to Fe(III)(oxyhydr)oxides~~ (Kappler et al., 2005; Weber et al.,

Ernest Chi Fru 5/4/2018 04:39

Deleted: conditions

Ernest Chi Fru 5/4/2018 04:32

Deleted: characterized by a

Ernest Chi Fru 5/4/2018 03:36

Deleted: high

Ernest Chi Fru 5/4/2018 03:35

Deleted: bottom water content

Ernest Chi Fru 5/4/2018 03:45

Deleted: concentrations

Ernest Chi Fru 5/4/2018 03:46

Deleted: ((Ozawa et al., 2016;

Ernest Chi Fru 5/4/2018 03:46

Moved (insertion) [1]

Ernest Chi Fru 5/4/2018 03:48

Deleted:)

Ernest Chi Fru 5/4/2018 05:02

Deleted: strict

Ernest Chi Fru 5/4/2018 04:26

Deleted: s

Ernest Chi Fru 5/4/2018 04:24

Deleted: such

Ernest Chi Fru 4/4/2018 23:21

Deleted: extremely difficult to attain uncommon

Ernest Chi Fru 5/4/2018 04:28

Deleted: modern

Ernest Chi Fru 5/4/2018 03:20

Deleted: demonstrated

Ernest Chi Fru 5/4/2018 03:01

Deleted: The precipitation of

Ernest Chi Fru 5/4/2018 03:01

Deleted: requires

Ernest Chi Fru 5/4/2018 03:12

Deleted: the

Ernest Chi Fru 5/4/2018 03:12

Deleted: of oxygen

Ernest Chi Fru 5/4/2018 03:02

Deleted: is not oxidized

Ernest Chi Fru 5/4/2018 03:13

Deleted: , while light and photoferrotrophy will oxidize reduced Fe to Fe(III)(oxyhydr)oxides. Both light and photoferrotrophy are however extremely rare characteristics of anoxic sediments,

Ernest Chi Fru 5/4/2018 03:10

Deleted: but a common feature of anoxic Fe²⁺-rich waters, where photoferrotrophy is widespread

1020 2006). Collectively, these observations provide an important feasible
1021 mechanism for the knife sharp separation of the Mn oxide-rich ores in the
1022 CVSB that are also Fe(III)(oxyhydr)oxide-rich, from the highly localized
1023 MFIF and NFIF deposits that are Fe(III)(oxyhydr)oxide-rich but Mn oxide-
1024 poor.

1025 5. The mechanism of formation of the MFIF and NFIF therefore most likely
1026 involved exhalative release of reduced hydrothermal/volcanic fluids into a
1027 restricted and deoxygenated seafloor water column where the oxidation of
1028 reduced Fe to Fe(III)(oxyhydr)oxides occurred, most likely by the activity of
1029 photoferrotrophs (Chi Fru et al., 2013). Microaerophilic oxidation of Fe(II)
1030 was likely critical, but that remains to be explored.

1031 6. Episodic intensification of hydrothermal activity is identified as a main
1032 mechanism for the formation of the millimetric BIF bands, adding to the
1033 biological mechanism that was inferred from fossil records in the MFIF (Chi
1034 Fru et al., 2013, 2015).

1035 7. Abiotic Si precipitation was much slower relative to Fe(III) precipitation,
1036 resulting in Fe-rich bands in the NFIF forming in association with large
1037 fragments of volcanoclast and the Si-rich bands with finer Si grains.

1038 8. A combination of the above processes produced pulses of Si and Fe in the
1039 millimetric Si and Fe-rich bands in the NFIF.

1040 9. Whether the rocks described here are analogs of Precambrian BIFs or not, and
1041 whether the proposed formation mechanisms match those that formed the
1042 ancient rocks, is opened to debate. However, there are many similarities to
1043 proposed Precambrian BIF depositional models (e.g. Klien, 2005; Beukes and
1044 Gutzmer, 2008; Smith et al., 2013; Bekker et al., 2010; Klein and Beukes,

Ernest Chi Fru 5/4/2018 03:53

Deleted: shown

Ernest Chi Fru 5/4/2018 04:21

Deleted: <#>The Milos rocks fulfill sedimentological, chemical and mineralogical characteristics that established them as potentially the youngest known BIFs; following the simplistic definition that BIFs are sedimentary rocks composed of alternating layers of Fe and Si containing at least 15% Fe. .

1054 1992). Importantly, the present study provides mechanisms by which rocks
1055 with alternating Fe and Si-rich bands can be formed in the modern ocean.

1056

1057 *Data availability.* Data can be accessed by request from any of the authors

1058

1059 *Author contributions.* ECF, SK and MI designed the study. ECF, SK, KG and MI
1060 performed fieldwork. ECF, JER, KG, IM and QH performed research. ECF, SK, KG,
1061 MI, QH and JER interpreted data. ECF and SK wrote paper.

1062

1063 *Competing interests.* The authors declare that they have no conflict of interest.

1064

1065 *Acknowledgments.* Ariadne Argyraki, Nicole Posth, Nolwenn Callac and Eva Zygouri
1066 are acknowledged field assistance during sampling and for stimulating intellectual
1067 discussions. Special thanks to Christoffer Hemmingsson for contributing to the SEM
1068 and XRD analyses. Christophe Brosson is acknowledged for his work on sequential
1069 iron extraction. This work is funded by the European Research Council (ERC)
1070 Seventh Framework Program (FP7) grant No. 336092 and the Swedish Research
1071 Council grant No. 2012-4364.

1072

1073

1074

1075

1076

1077

1078

1079

1080

1081

1082

1083

1084 **References**

1085 Alain, K., Holler, T., Musat, F., Elvert, M., Treude, T., and Kruger M.;

1086 Microbiological investigation of methane- and hydrocarbon-discharging mud

1087 volcanoes in the Carpathian Mountains, Romania. *Environ. Microbiol.*, 8, 574–

1088 590, 2006.

1089 Alfieris, D. and Voudouris, P.: Ore mineralogy of transitional submarine magmatic-

1090 hydrothermal deposits in W. Milos Island, Greece. *Bul. Acad. Sci.*, 43, 1–6, 2005.

1091 Alfieris, D.; Geological, geochemical and mineralogical studies of shallow submarine

1092 epithermal mineralization in an emergent volcanic edifice, at Milos Island (western

1093 side), Greece. PhD thesis, Department Geowissenschaften der Universität

1094 Hamburg, 2006.

1095 Alfieris, D., Voudouris, P., and Spry, P.: Shallow submarine epithermal Pb–Zn–Cu–

1096 Au–Ag–Te mineralization on western Milos Island, Aegean Volcanic Arc, Greece:

1097 Mineralogical, geological and geochemical constraints. *Ore Geol. Rev.*, 53, 159–

1098 180, 2013.

1099 Anand, R. R., Paine, M., and Smith, R.E.: Genesis, Classification and Atlas of

1100 Ferruginous Materials, Yilgarn Craton. CRC LEME Open File Report vol. 13,

1101 CSIRO Exploration and Mining, Perth, 2002.

1102 Bahlburg, H. and Dobrzinski, N.: A review of the Chemical Index of Alteration (CIA)
 1103 and its application to the study of Neoproterozoic glacial deposits and climate
 1104 transition. *Geol. Soc. London Mem.*, 36, 81–92, 2011.

1105 Bau, M. and Dulski, P.: Distribution of yttrium and rare- earth elements in the Penge
 1106 and Kuruman Iron-Formations, oxidative scavenging of cerium on hydrous Fe
 1107 oxide, Transvaal Supergroup, South Africa. *Precambrian Res.*, 79, 37–55, 1996.

1108 Berg, I.A., Kockelkorn, D., Ramos-Vera, W.H., Say, R.F., Zarzycki, J., Hügler, M.,
 1109 Alber, B.E., and Fuchs, G.: Autotrophic carbon fixation in archaea. *Nat. Rev.*
 1110 *Microbiol.*, 8, 447–460, 2010.

1111 Bekker, A., Slack J.F., Planavsky, N., Krapež B., Hofmann, A., Konhauser, K.O., and
 1112 Rouxel, O.J.: Iron formation: The sedimentary product of a complex interplay
 1113 among mantle, tectonic, oceanic, and biospheric processes. *Econ. Geol.*, 105, 467–
 1114 508, 2010.

1115 Beukes, N.J., and Gutzmer, J.: Origin and Paleoenvironmental significance of major
 1116 Iron Formations at the Archean-Paleoproterozoic boundary. *Econ. Geol.* 15, 5–47,
 1117 2008.

1118 Beukes, N.J., Swindell, E.P.W., Wabo, H.: Manganese deposits of Africa, Episodes v.
 1119 39, 285–317, 2016.

1120 Blumenberg, M., Seifert, R., Reitner, J., Pape, T., and Michaelis, W.: Membrane lipid
 1121 patterns typify distinct anaerobic methanotrophic consortia. *Proc. Natl. Acad. Sci.*
 1122 *U.S.A.*, 101, 11111–11116, 2004.

1123 Boström, K., Honnorez, J., Joensuu, O., and Rydell, H.: Chemistry of hydrothermal
 1124 solutions in drill hole GPK-1, Palaea Kameni, Santorini, Greece. *Proceedings of*
 1125 *the third international congress, Santorini, Greece.* 3, 257–260, 1990.

1126 Bronn, H.G.: Übersicht der Fossilen Überreste in den tertiären subappenninischen
 1127 Gebirgen. Italiens Tertiär-Gebilde und deren organische Einschlüsse. Heidelberg
 1128 pp. XII + 176 + 1 pl, 1831.
 1129 Bouma, A.H.: Sedimentology of Some Flysch Deposits. Amsterdam, Elsevier, pp.
 1130 168, 1962.
 1131 Breitzkreuz, C.: Spherulites and lithophysae—200 years of investigation on
 1132 hightemperature crystallization domains in silica-rich volcanic rocks. Bull.
 1133 Volcanol., 75, 1–16, 2013.
 1134 Bühring, S.I., Elvert, M., and Witte, U.: The microbial community structure of
 1135 different permeable sandy sediments characterized by the investigation of bacterial
 1136 fatty acids and fluorescence in situ hybridization. Environ. Microbiol., 7, 281–293,
 1137 2005.
 1138 Callac, N., Posth, N.R., Rattray, J.E., Yamoah, K.K.Y., Wiech, A., Ivarsson, M.,
 1139 Hemmingsson, C., Kiliass, S.P., Argyraki, A., Broman, C., Skogby, H.,
 1140 Smittenberg, R.H., and Chi Fru, E.: Modes of carbon fixation in an arsenic and
 1141 CO₂-rich shallow hydrothermal ecosystem. Sci. Rep., 7, 14708,
 1142 doi:10.1038/s41598-017-13910-2, 2017.
 1143 Camilli, R., Noumiku P., Escartin, J., Ridao, P., Mallios, A., Kiliass, S.P., Argyraki,
 1144 A., and the Caldera Science Team: The Kallisti Limnes, carbon dioxide
 1145 accumulating subsea pools. Sci. Rep., 5, 12152, doi:10.1038/srep12152, 2015.
 1146 Canuel, E.A. and Marten, C.S.: Reactivity of recently deposited organic matter:
 1147 Degradation of lipid compounds near the sediment-water interface. Geochim.
 1148 Cosmo. Acta, 60, 1793–1806, 1996.

1149 Canet, C., Prol-Ledesma, R.M., Torres-Alvarado, I., Gilg, H.A., Villanueva, R.E., and
 1150 Cruz, R.L.S.: Silica-carbonate stromatolites related to coastal hydrothermal venting
 1151 in Bahia Concepcion, Baja California Sur, Mexico. *Sed. Geol.*, 174, 97–113, 2005.
 1152 Cattaneo, A. and Steel, R.J.: Transgressive deposits: a review of their variability.
 1153 *Earth Sci. Rev.*, 62, 187–228, 2003.
 1154 Chi Fru, E., Piccinelli, P., and Fortin, D.: Insights into the global microbial
 1155 community structure associated with iron oxyhydroxide minerals deposited in the
 1156 aerobic biogeosphere. *Geomicrobiol. J.*, 29, 587–610, 2012.
 1157 Chi Fru, E., Ivarsson, M., Kiliyas, S.P., Bengtson, S., Belivanova, V., Marone, F.,
 1158 Fortin, D., Broman, C., and Stampanoni, M.: Fossilized iron bacteria reveal a
 1159 pathway to the origin banded iron formations. *Nat. Comm.*, 4, 2050 DOI:
 1160 10.1038/ncomms3050, 2013.
 1161 Chi Fru, E., Ivarsson, M., Kiliyas, S.P., Frings, P.J., Hemmingsson, C., Broman, C.,
 1162 Bengtson, S. and Chatzitheodoridis, E.: Biogenicity of an Early Quaternary iron
 1163 formation, Milos Island, Greece. *Geobiology*, 13, 225–44, 2015.
 1164 Dando, P.R., Hughes, J.A., Leahy, Y., Niven, S.J., Taylor, L.J. and Smith, C.: Gas
 1165 venting rates from submarine hydrothermal areas around the island of Milos,
 1166 Hellenic Volcanic Arc. *Cont. Shelf Res.*, 15, 913–925, 1995.
 1167 Dieke, P. Concentration of Mn and separation from Fe in sediments—I. Kinetics and
 1168 stoichiometry of the reaction between birnessite and dissolved Fe(II) at 10°C.
 1169 *Geochim. Cosmo. Acta*, 49, 1023–1033, 1985.
 1170 Dorr, J.V.N.: Supergene iron ores of Minas Gerais, Brazil. *Econ. Geol.*, 59, 1203,
 1171 1964.

1172 Dowling, N.J. E., Widdel, F., and White, D.C.: Phospholipid ester-linked fatty-acid
 1173 biomarkers of acetate-oxidizing sulfate-reducers and other sulfide-forming
 1174 bacteria. *J. Gen. Microbiol.*, 132, 1815–1825, 1986.
 1175 Drüitt, T. H. L., Edwards, R. M., Mellors, D. M., Pyle, R. S. J., Sparks, M., Lanphere,
 1176 M. D., and Barreiro, B.: Santorini Volcano. *Geol. Soc. Mem. London*, 19, 165,
 1177 1999.
 1178 Fischer, W.W. and Knoll, A.H.: An iron shuttle for deepwater silica in Late Archean
 1179 and early Paleoproterozoic iron formation. *Geol. Soc. Am. Bull.*, 121, 222–235,
 1180 2009.
 1181 Franco, A.C., Hernández-Ayón, J.M., Beier E., Garçon, V., Maske, H., Paulmier, A.,
 1182 Färber-Lorda, J., Castro, R., and Sosa-Ávalos, R.: Air-sea CO₂ fluxes above the
 1183 stratified oxygen minimum zone in the coastal region off Mexico. *J. Geophys. Res.*,
 1184 119, 2923–2937, 2014.
 1185 Friedrich, W.L., Kromer, B., Friedrich, M., Heinemeier, J., Pfeiffer, T., and Talamo,
 1186 S.: Santorini eruption radiocarbon dated to 1627-1600 BC. *Science*, 312, 548–548,
 1187 2006.
 1188 Fytikas, M., Innocenti, F., Kolios, N., Manetti, P., Mazzuoli, R., Poli, G., Rita, F., and
 1189 Villari, L.: Volcanology and petrology of volcanic products from the island of
 1190 Milos and Neighbouring islets. *J. Vol. Geotherm. Res.*, 28, 297–317, 1986.
 1191 Galan, L.D.P., Doval, M., La Iglesia, A., Soriano, J., and Chavez, L.: Occurrence of
 1192 silica polymorphs nanocrystals in tuffaceous rocks, Province of the Mesa Central,
 1193 Mexico, and their formation from subcritical Si-rich fluids. *Am. Mineral.*, 98, 977–
 1194 985, 2013.
 1195 Georgalas, G., and Liatsikas, N.: Die Historische entwicklung des Dafni-Ausbruches
 1196 1925-1926. In Santorin, Der Werdegang eines Inselvulkans und sein Ausbruch

1197 1925-1928, V. 2 (ed. Reck, H.). Verlag von Dietrich Reimer, Berlin, 1–96 pp,
 1198 1936.

1199 Glasby, G.P. and Schulz, H.D.: Eh, pH diagrams for Mn, Fe, Co, Ni, Cu and As under
 1200 seawater conditions: application of two new types of the Eh, pH diagrams to the
 1201 study of specific problems in marine geochemistry. *Aquatic Geochem.*, 5, 227–
 1202 248, 1999.

1203 Glasby, G.P., Papavassiliou, C.T., Mitsis, J., and Valsami-Jones, E.: The Vani
 1204 manganese deposit, Milos island, Greece: A fossil stratabound
 1205 Mn–Ba–Pb–Zn–As–Sb–W-rich hydrothermal deposit. *Develop. Volcanol.*, 7,
 1206 255–291, 2005.

1207 Gromet, L.P., Dymek, R.F., Haskin, L.A., and Korotev, R.L.: The North American
 1208 shale composi: Its compilation and major trace element characteristics. *Geochim.*
 1209 *Cosmo. Acta*, 48, 2469–2482, 1984.

1210 Gross, G.A.: A classification of iron-formation based on depositional Environments.
 1211 *Can. Min.*, 18, 215–222, 1980.

1212 Guilbaud, R., Poulton, S.W., Butterfield, N.J., Zhu, M., and Shields-Zou, G.A.: A
 1213 global transition to ferruginous conditions during the early Neoproterozoic. *Nat.*
 1214 *Geosci.* 8:466–470, 2015.

1215 Handley, K. M., Boothman, C., Mills, R. A., Pancost, R. D., and Lloyd, J. R.:
 1216 Functional diversity of bacteria in a ferruginous hydrothermal sediment. *ISME J.*,
 1217 4, 1193-1205, 2010.

1218 Hanert, H. H.: Bacterial and chemical iron oxide deposition in a shallow bay on
 1219 Palaea Kameni, Santorini, Greece: microscopy, electron probe microanalysis, and
 1220 photometry of in situ experiments. *Geomicrobiol. J.*, 19, 317–342, 2002.

- 1221 Hein, J. R., Stamatakis, M. G., and Dowling, J. S.: Trace metal-rich Quaternary
1222 hydrothermal manganese oxide and barite deposit, Milos Island, Greece. *Applied*
1223 *Earth Science: Trans. Inst. Min. Metal. Section B.*, 109, 67–76, 2000.
- 1224 Hoffman, P. F., Kaufman, A. J., Halverson, G. P., and Schrag, DP.: A Neoproterozoic
1225 Snowball Earth. *Science* 281, 1342-1346, 1998.
- 1226 Horwell, C.J., le Blond, S., Michnowicz, S. A. K. and Cressey, G.: Cristobalite in a
1227 rhyolitic lava dome: evolution of ash hazard. *Bull. Volcanol.* 72, 249-253, 2010.
- 1228 Ichihara, K. and Fukubayashi, Y.: Preparation of fatty acid methyl esters for gas-
1229 liquid chromatography. *J. Lipid Res.*, 51, 635–40, 2010.
- 1230 James, H. L.: Sedimentary facies of iron-formation. *Econ. Geol.*, 49, 235–293, 1954.
- 1231 Johnson, C. M., Beard, B. L., and Roden, E. E.: The iron isotope fingerprints of redox
1232 and biogeochemical cycling in modern and ancient Earth. *Ann. Rev. Earth Plan.*
1233 *Sci.*, 36, 457–493, 2008.
- 1234 Kappler, A., Pasquero, C., and Newman, D.K.: Deposition of banded iron formations
1235 by anoxygenic phototrophic Fe(II)-oxidizing bacteria. *Geology*, 33, 865–868,
1236 2005.
- 1237 Kiliyas, S. P., Detsi, K., Godelitsas, A., Typas, M., Naden, J., and Marantos, Y.:
1238 Evidence of Mn-oxide biomineralization, Vani Mn deposit, Milos, Greece. In:
1239 *Proceedings of the ninth biennial Meeting of the Society for Geology Applied to*
1240 *Mineral Deposits, Dublin, Ireland. Irish Assoc. Econ. Geol.* 1069–1072 pp, 2007.
- 1241 Kiliyas, S. P.: Microbial mat-related structures in the Quaternary Cape Vani
1242 manganese-oxide (-barite) deposit, NW Milos island, Greece. *Soc. Sed. Geol. Sp.*
1243 *Pub.*, 101, 97–110, 2011.

1244 Kiliyas, S. P., Chatzitheodoridis, E., and Lyon, I.: Molecular, chemical and
1245 morphological evidence for hematite biogenicity at the Quaternary Cape Vani Mn-
1246 (Ba-Fe) deposit, Milos, Greece. *Bull. Geol. Soc.*, 47, 834-842, 2013a.

1247 Kiliyas, P. S., Nomikou, P., Papanikolaou, D., Polymenakou, P. N., Godelitsas, A.,
1248 Argyraki, A., Carey, S., Gamaletsos, P., Mertzimekis, T. J., Stathopoulou, E.,
1249 Goettlicher, J., Steininger, R., Betzelou, K., Livanos, I., Christakis, C., Bell, K. C.:
1250 and Scoullou, M. New insights into hydrothermal vent processes in the unique
1251 shallow-submarine arc-volcano, Kolumbo (Santorini), Greece. *Sci. Rep.*, 3,
1252 doi:10.1038/srep02421, 2013b.

1253 Klein, C.: Some Precambrian banded iron-formations (BIFs) from around the world:
1254 Their age, geologic setting, mineralogy, metamorphism, geochemistry, and origins.
1255 *Am. Min.*, 90, 1473–1499, 2005.

1256 Kling, G. W., Evans, W. C., Tanyileke, G., Kusakabe, M., Ohba, T., Yoshida, Y., and
1257 Hell, J. V.: Degassing Lakes Nyos and Monoun: Defusing certain disaster. *Proc.*
1258 *Natl. Acad. Sci. U.S.A.*, 102, 14185–14190, 2005.

1259 Klein, C., and Beukes, N.J.: Time distribution, stratigraphy and sedimentologic
1260 setting, and geochemistry of Precambrian Iron Formation. In Schopf, J. W., and
1261 Klein, C.: *The Proterozoic Biosphere: A multidisciplinary study*, 139 – 146.
1262 Cambridge University Press, New York, 1992.

1263 Konhauser, K. O., Planavsky, N. J., Hardisty, D. S., Robbins, L. J., Warchola, T. J.,
1264 Haugaard, R., Lalonde, S. V., Partin, C. A., Oonk, P. B. H., Tsikos, H., and Lyons,
1265 T.W.: Iron formations: A global record of Neoproterozoic to Palaeoproterozoic
1266 environmental history. *Earth Sci. Rev.*, 172, 140-177, 2017.

1267 Krapež, B., Barley, M. E., Pickard, A. L.: Hydrothermal and resedimented origins of
1268 the precursor sediments to banded iron formations: Sedimentological evidence

1269 from the early Palaeoproterozoic Brockman Supersequence of Western Australia.
 1270 Sedimentology, 50, 979-1011, 2003.

1271 Lalonde, K., Mucci, A., Quellet, A. and G  linas, Y.: Preservation of organic matter in
 1272 sediments promoted by iron. Nature, 483, 198–200, 2012.

1273 Levett, A., Gagen, E., Shuster, J., Rintoul, L., Tobin, M., Vongsvivut, J., Bambery,
 1274 K., Vasconcelos, P., and Southam, G.: Evidence of biogeochemical processes in
 1275 iron duricrust formation. J. South. Am. Earth Sci., 71, 131–142, 2016.

1276 Li, W., Czaja, A. D., Van Kranendonk, M. J., Beard, B. L., Roden, E. E., Johnson, C.
 1277 M.: An anoxic, Fe(II)-rich, U-poor ocean 3.46 billion years ago. Geochim. Cosmo.
 1278 Acta, 120, 65-79, 2013.

1279 Liakopoulos, A., Glasby, G. P., Papavassiliou, C. T. and Boulegue, J.: Nature and
 1280 origin of the Vani manganese deposit, Milos, Greece: an overview. Ore Geol. Rev.,
 1281 18, 181–209, 2001.

1282 L  , D., Song, Q., and Wang, X.: Decomposition of algal lipids in clay-enriched
 1283 marine sediment under oxic and anoxic conditions. Chin. J. Oceanogr. Limnol., 28,
 1284 131–143, 2010.

1285 Marschik, R., Bauer, T., Hensler, A.-S., Skarpelis, N., and H  lzl, S. Isotope
 1286 Geochemistry of the Pb-Zn-Ba(-Ag-Au) Mineralization at Triades-Galana, Milos
 1287 Island, Greece. Res. Geol., 60, 335–347, 2010.

1288 Maynard, J. B.: Chemistry of modern soils as a guide to interpreting Precambrian
 1289 Paleosols. J. Geol., 100, 279–289, 1993.

1290 Maynard, J. B.: The chemistry of manganese ores through time: a signal of increasing
 1291 diversity of earth-surface environments. Econ. Geol., 105, 535–552, 2010.

1292 McLennan, S.B.: Rare earth elements in sedimentary rocks. Influence of provenance
 1293 and sedimentary processes. In: B.R. Lipin and G.A. McKay (Editors),

1294 Geochemistry and Mineralogy of the Rare Earth Elements. Mineralogical Society
 1295 of America, Washington, pp. 169-200, 1989.

1296 Miall, A. D. Lithofacies types and vertical profile models in braided river deposits.
 1297 Can. Soc. Pet. Geol. Mem., 5, 597–604, 1978.

1298 Miall, A. D.: Architectural element analysis: a new method of facies analysis applied
 1299 to fluvial deposits. Earth Sci. Rev., 22, 261–308, 1985.

1300 Morris, R. V., Vaniman, D. T., Blake, D. F., Gellert, R., Chipera, S. J., Rampe, E. B.,
 1301 Ming, D. W., Morrison, S. M., Downs, R. T., Treiman, A. H., Yen, A. S.,
 1302 Grotzinger, J. P., Achilles, C. N., Bristow, T. F., Crisp, J. A., Des Marais, D. J.,
 1303 Farmer, J. D., Fendrich, K. V., Frydenvang, J., Gradd, T. G., Morookian, J.-M.,
 1304 Stolper, E. M. and Schwenzer, S. P.: Silicic volcanism on Mars evidenced by
 1305 tridymite in high-SiO₂ sedimentary rock at Gale crater. Proc. Natl. Acad. Sci.
 1306 U.S.A., 113, 7071–7076, 2016.

1307 Mutti, E.: Turbidite Sandstones. Agip Spe. Pub., 275 pp, 1992.

1308 Nesbitt, H. W. and Young, G. M.: Early Proterozoic climates and plate motions
 1309 inferred from major element chemistry of lutites. Nature, 199, 715–717, 1982.

1310 Nomikou, P., Papanikolaou, D., Alexandri, M., Sakellariou, D., and Rousakis, G.:
 1311 Submarine volcanoes along the Aegean volcanic arc. Tectonophysics, 597–598,
 1312 123–146, 2013.

1313 Nomikou, P., Parks, M. M., Papanikolaou, D., Pyle, D. M., Mather, T. A., Carey, S.,
 1314 Watts, A. B., Paulatto, M., Kalnins, M.L., Livanos, I., and Bejelou, K.: The
 1315 emergence and growth of a submarine volcano: The Kameni islands, Santorini
 1316 (Greece). Geo. Res. J., 1, 8–18, 2014.

1317 Ozawa, A., Ueda, A., Fantong, W. Y., Anazawa, K., Yoshida, Y., Kusakabe, M.,
 1318 Ohba, T., Tanyileke, G., and Hell, J.V. Rate of siderite precipitation in Lake Nyos,
 1319 Cameroon. *Geol. Soc. London Sp. Pub.*, 437, doi.org/10.1144/SP437.13, 2016.
 1320 Papanikolaou, D., Lekkas, E., and Syskakis, D.: Tectonic analysis of the geothermal
 1321 field of Milos Island. *Bull. Geol. Soc. Greece*, 24, 27–46, 1990.
 1322 Papavassiliou, K., Voudouris, P., Kanellopoulos, C., Glasby, G., Alfieris, D., and
 1323 Mitsis, I.: New geochemical and mineralogical constraints on the genesis of the
 1324 Vani hydrothermal manganese deposit at NW Milos island, Greece: Comparison
 1325 with the Aspro Gialoudi deposit and implications for the formation of the Milos
 1326 manganese mineralization. *Ore Geol.*, 80, 594–611, 2017.
 1327 Paulmier, A., Ruíz-Pino, D., and Garçon, V.: The oxygen minimum zone (OMZ) off
 1328 Chile as intense source of CO₂ and N₂O, *Cont. Shelf. Res.*, 28, 2746–2756, 2008.
 1329 Paulmier, A., Ruiz-Pino, D., and Gaçon, V.: CO₂ maximum in the oxygen minimum
 1330 zone (OMZ). *Biogeosciences*, 8, 239–252. doi:10.5194/bg-8-239-2011, 2011.
 1331 Percoits, E., Gingras, M. K., Barley, M. E., Kapper, A., Posth, N. R., and Konhauser,
 1332 K.O.: Petrography and geochemistry of the Dales Gorge banded iron formation:
 1333 Paragenetic sequence, source and implications for palaeo-ocean chemistry. *Pre.*
 1334 *Res.*, 172, 2009.
 1335 Pichler, T. and Dix, G. R. Hydrothermal venting within a coral reef ecosystem,
 1336 Ambitle Island, Papua New Guinea. *Geology*, 50, 435–438, 1996.
 1337 Pichler, T. and Veizer, J.: Precipitation of Fe(III) oxyhydroxide deposits from
 1338 shallow-water hydrothermal fluids in Tutum Bay, Ambitle Island, Papua New
 1339 Guinea. *Chem. Geol.*, 162, 15–31, 1999.

1340 Pichler, T. and Veizer, J. The precipitation of aragonite from shallow-water
1341 hydrothermal fluids in a coral reef, Tutum Bay, Ambitle Island, Papua New
1342 Guinea. *Chem. Geol.*, 207, 317–45, 2004.

1343 Planavsky, N., Rouxel, O., Bekker, A., Shapiro, R., Fralick, P., and Knudsen, A.:
1344 Iron-oxidizing microbial ecosystems thrived in late Paleoproterozoic redox-
1345 stratified oceans. *Earth Plan. Sci. Letts.*, 286, 2307–242, 2009.

1346 Planavsky, N. J., Bekker, A., Rouxel, O. J., Kamber, B., Hofmann, A., Knudsen, A.
1347 and Lyons T. W.: Rare earth element and yttrium compositions of Archean and
1348 Paleoproterozoic Fe formations revisited: New perspectives on the significance
1349 and mechanisms of deposition. *Geochim. Cosmo. Acta*, 74, 6387–6405, 2010.

1350 Plimer, I. *Milos Geologic History*. Koan Publishing House, Athens, Greece. 261 pp,
1351 2000.

1352 Poulton, S.W., and Canfield, D.E.: Development of a sequential iron extraction
1353 procedure for iron: implications for iron partitioning in continentally derived
1354 particles. *Chem. Geol.* 2014, 209–221, 2005.

1355 Poulton, S.W. and Canfield, D.E.: Ferruginous conditions: A dominant feature of the
1356 ocean through Earth's history. *Elements*. 7, 107–112, 2011.

1357 Preuß, A., Schauder, R., Fuchs, G., and Stichler W.: Carbon isotope fractionation by
1358 autotrophic bacteria with three different CO₂ fixation pathways. *Zeitschrift für*
1359 *Naturforschung C.*, 44, 397–402, 1989.

1360 Rancourt, D. G., Fortin, D., Pichler, T., and Lamarche, G.: Mineralogical
1361 characterization of a natural very As-rich hydrous ferric oxide coprecipitate formed
1362 by mixing of hydrothermal fluid and sea water. *Am. Min.*, 86, 834–851, 2001.

1363 Rasmussen, B., Meier, D. B., Krapež. B., and Muhling, J. R.: Iron silicate
 1364 microgranules as precursor sediments to 2.5-billion-year-old banded iron
 1365 formations. *Geology*, 41, 435–438, 2013.

1366 Rasmussen, B., Krapež, B., and Meier, D. B. Replacement origin for hematite in 2.5
 1367 Ga banded iron formation: Evidence for postdepositional oxidation of iron-bearing
 1368 minerals. *Geol. Soc. Am. Bull.*, 126, 438–446, 2014.

1369 Riedel, T., Zak, D., Biester, H., and Dittmar, T.: Iron traps terrestrially derived
 1370 dissolved organic matter at redox interfaces. *Proc. Nat. Acad. Sci. U.S.A.*, 110,
 1371 10101–10105, 2013.

1372 Robbins, E. I., Kourtidou-Papadeli, C., Iherall, A. S., Nord, Jr, G. L. and Sato, M.:
 1373 From Precambrian Iron-Formation to Terraforming Mars: The JIMES Expedition
 1374 to Santorini. *Geomicrobiol. J.*, 33, 630–645, 2016.

1375 Roy, S.: Manganese Mineralization: Geochemistry and mineralogy of terrestrial and
 1376 marine deposits. *Geol. Soc. Spe. Pub.*, 119, 5–27, 1997.

1377 Roy, S.: Sedimentary manganese metallogenesis in response to the evolution of the
 1378 Earth system. *Earth-Sci. Rev.*, 77, 273–305, 2006.

1379 Rudnick, R. and Gao, S. Composition of the continental crust. In: *Treatise on*
 1380 *Geochemistry*, vol. 3. Elsevier–Pergamon, Oxford, 1–64 pp, 2003.

1381 Shanmugam, G.: Submarine fans: a critical retrospective (1950–2015). *J.*
 1382 *Palaeogeogr.*, 5, 110–184, 2016.

1383 Schwertmann, U. and Murad, E. Effect of pH on the formation of goethite and
 1384 hematite from ferrihydrite. *Clay Clay Min.*, 31, 277–284, 1983.

1385 Shuster, D. L., Farley, K. A., Vasconcelos, P. M., Balco, G., Monteiro, H. S.,
 1386 Waltenberg, K., and Stone, J. O. Cosmogenic ^3He in hematite and goethite from

1387 Brazilian “canga” duricrust demonstrates the extreme stability of these surfaces.
 1388 Earth Plan. Sci. Lett., 329, 41–50, 2012.
 1389 Sigurdsson, H., Carey, S., Alexandri, M., Vougioukalakis, G., Croff, K., Roman, C.,
 1390 Sakellariou, D., Anagnostou, C., Rousakis, G., Loakim, C., Goguo, A., Ballas, D.,
 1391 Misaridis, T., and Nomikou, P. Marine investigations of Greece’s Santorini
 1392 volcanic field. EOS Trans. Am. Geophy. Union, 87, 337–342, 2006.
 1393 Simonson, B. M.: Sedimentological constraints on the origins of Precambrian iron-
 1394 formations. Geol. Soc. Am. Bull., 96, 244–252, 1985.
 1395 Simonson, B. M. and Hassler, S. W.: Was the deposition of large Precambrian iron
 1396 formations linked to major marine transgressions? The J. Geol., 104, 665–676,
 1397 1996.
 1398 Skarpelis, N. and Koutles, T.: Geology of epithermal mineralization of the NW part of
 1399 Milos Island, Greece. In Proceedings of the 5th International Symposium on
 1400 Eastern Mediterranean Geology. (eds. Chatzipetros, A. & Pavlides S). School of
 1401 Geology, Aristotelian University of Thessaloniki, Thessaloniki, Greece. pp. 1449–
 1402 1452, 2004.
 1403 Smith, A.J.B., Beukes, N.J., and Gutzmer, J.: The Composition and depositional environments of
 1404 Mesoarchean Iron Formations of the West Rand Group of the Witwatersrand Supergroup, South
 1405 Africa. Econ. Geol. 108, 111–134, 2013.
 1406 Sperling, E.A., Wolock, C.J., Gill, B.C., Kunzmann, M., Halverson, G.P., Macdonald,
 1407 F.A., Knoll, A.H., and Johnston D.T.: Statistical Analysis of Iron Geochemical
 1408 Data Suggests Limited Late Proterozoic Oxygenation. Nature 523, 451–454, 2015.
 1409 Stewart, A. L. and Mcphie, J.: Facies architecture and Late Pliocene – Pleistocene
 1410 evolution of a felsic volcanic island, Milo, Greece. Bull. Volcanol. 68, 703–726,
 1411 2006.

1412 Sun, S., Konhauser, K. O., Kappler, A., and Li, Y.-L.: Primary hematite in
 1413 Neoproterozoic to Paleoproterozoic oceans. *GSA Bull.*, 127, 850–861, 2015.
 1414 Stüben, D. and Glasby, G.P.: Geochemistry of shallow submarine hydrothermal fluids
 1415 from Paleohori Bay, Milos, Aegean Sea. *Exp. Min. Geol.*, 8, 273–287, 1999.
 1416 Swamy, V., Saxena, S. K., Sundman, B., and Zhang, J.: A thermodynamic assessment
 1417 of silica phase diagram. *J. Geophys. Res. Solid Earth*, 99, 11787–11794, 1994.
 1418 Taylor, J., and Parkes, R. J.: The cellular fatty-acids of the sulfate-reducing bacteria,
 1419 *Desulfobacter* sp., *Desulfobulbus* sp. and *Desulfovibrio desulfuricans*. *J. Gen.*
 1420 *Microbiol.*, 129, 3303–3309, 1983.
 1421 Tice, M. M. and Lowe, D. R.: The origin of carbonaceous matter in pre-3.0 Ga
 1422 greenstone terrains: A review and new evidence from the 3.42 Ga Buck Reef
 1423 Chert. *Earth Sci. Rev.*, 76, 259–300, 2006.
 1424 Tiodjio, R. M., Sakatoku, A., Nakamura, A., Tanaka, A., Fantong, W. Y., Tchakam,
 1425 K. B., Tanyileke, G., Ohba, T., Hell, V. J., Kusakabe, M., Nakamura, S., and Ueda,
 1426 A.: Bacterial and archaeal communities in Lake Nyos (Cameroon, Central Africa).
 1427 *Sci. Rep.*, 4, 6151, DOI: 10.1038/srep06151, 2014.
 1428 Trendall, A.F.: The significance of iron-formation in the Precambrian stratigraphic
 1429 record. *Int. Assoc. Sed. Spe. Pub.*, 33, 33–66, 2002.
 1430 Tsikos, H., Mathews, A., Erel, Y., and Moore, J.M.: Iron isotopes constrain
 1431 biogeochemical redox cycling of iron and manganese in a Palaeoproterozoic
 1432 stratified basin. *Earth Planet. Sci. Lett.*, 298, 125–134, 2010.
 1433 van Hinsbergen, D. J. J., Snel, E., Garstman, S. A., Mărunțeanu, M., Langereis, C. G.,
 1434 Wortel, M. J. R., and Meulenkaamp, J. E.: Vertical motions in the Aegean volcanic
 1435 arc: evidence for rapid subsidence preceding volcanic activity on Milos and
 1436 Aegina. *Mar. Geol.*, 209, 329–345, 2004.

1437 Varnavas, S. P. and Cronan, D. S.: Submarine hydrothermal activity off Santorini and
1438 Milos in the Central Hellenic Volcanic Arc: A synthesis. *Chem. Geol.*, 224, 40–54,
1439 2005.

1440 Weber, K. A., Achenbach, L. A., and Coates, J. D.: Microorganisms pumping iron:
1441 anaerobic microbial iron oxidation and reduction. *Nat. Rev. Microbiol.*, 4, 752–64,
1442 2006.

1443

1444

1445

1446

1447

1448

1449

1450

1451

1452

1453

1454

1455

1456

1457

1458

1459

1460

1461

1462 Table 1. Table 1. Results of X-Ray Radiation (XRD) analysis showing major
1463 mineralogical compositions. NFIF (non-fossiliferous iron formation) and MFIF
1464 (microfossiliferous iron formation), respectively.

1465

Mineral phase	MFIF1	MFIF2	MFIF3	Fe-rich NFIF2A	Si-rich NFIF2B	Fe-rich NFIF2C	Si-rich NFIFD	Fe-rich NFIF2E	Fe-rich NFIF2F
Hematite	+	+	-	+	+	+	+	+	+
Quartz	+	+	+	-	-	-	-	-	-
Sanidine	-	-	-	+	+	+	+	+	+
Tridymite	-	-	-	-	+	+	+	+	+
Cristobalite	-	-	-	+	-	-	-	-	-
Cryptomelane	-	-	+	-	-	-	-	-	-

1466
1467
1468
1469
1470
1471
1472
1473
1474
1475
1476
1477
1478
1479
1480
1481
1482
1483
1484
1485
1486
1487
1488
1489
1490
1491
1492
1493
1494
1495
1496
1497
1498

1499 Table 2. Stable isotope results. Letters A-F on the NFIF samples represent respective
1500 bands of the sawn rock in Figure 7E.

Sample	$\delta^{13}\text{C}_{\text{org}}$ vs PDB (‰)	C_{org} (%)	$\delta^{15}\text{N}$ vs air (‰)	N (%)	$\delta^{34}\text{S}$ vs CDT (‰)	S (%)
Fe-rich NFIF2A	-25,63	0,061	nd	0,023	nd	0,01
Si-rich NFIF2B	-25,03	0,109	nd	0,017	nd	0,02
Fe-rich NFIF2C	-24,45	0,068	nd	0,013	nd	0,02
Si-rich NFIF2D	-25,04	0,076	nd	0,015	nd	0,02
Fe-rich NFIF2E	-25,19	0,042	nd	0,009	nd	0,01
Si-rich NFIF2F	-25,49	0,050	nd	0,012	nd	0,03
MFIF1	-25,49	0,087	nd	0,017	nd	0,01
MFIF2	-26,25	0,046	nd	0,005	nd	nd
MFIF3	-25,69	0,041	nd	0,006	nd	nd

ND, Not detected

1501
1502
1503
1504
1505
1506
1507
1508

1509

1510

1511

1512

1513

1514

1515

1516

1517

1518

1519

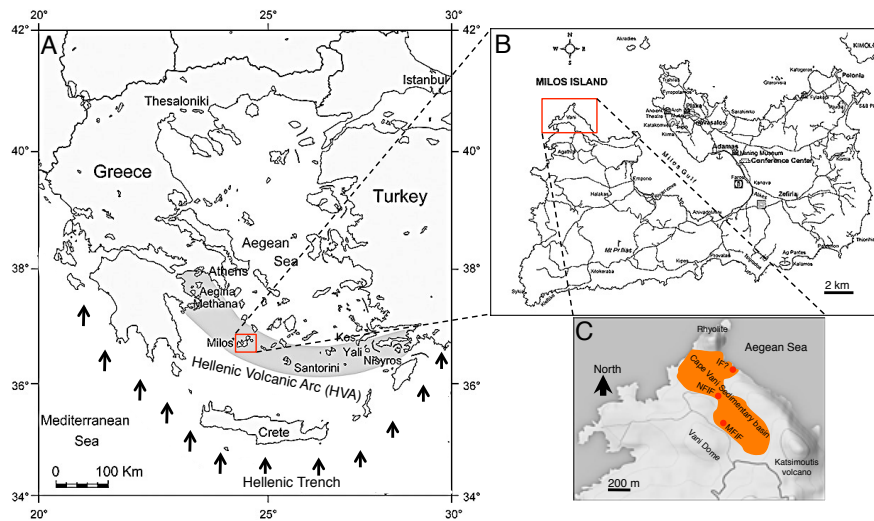


Fig. 1. Geological map of Milos (redrawn from Marschik et al., 2010). (A), Geotectonic map showing the position of Milos Island, along the Hellenic Volcanic Arc (HVA). Arrows indicate north east subduction of the African plate underneath the Euroasian plate. (B) Milos Island. (C), The Milos iron formation is located in the 8-shaped Cape Vani sedimentary basin (CVSB). At least two IFs are present in the CVSB. These are made up of a non-fossiliferous IF (NFIF) at the juncture between the two large sedimentary basins and a microfossiliferous IF (MFIF) located at the SW margin in the second basin. A potential third IF (IF?) is located to the NE, close to the present day Aegean Sea. It is however not certain if this deposit is part of the NFIF or not, because of the open mining pit separating the two.

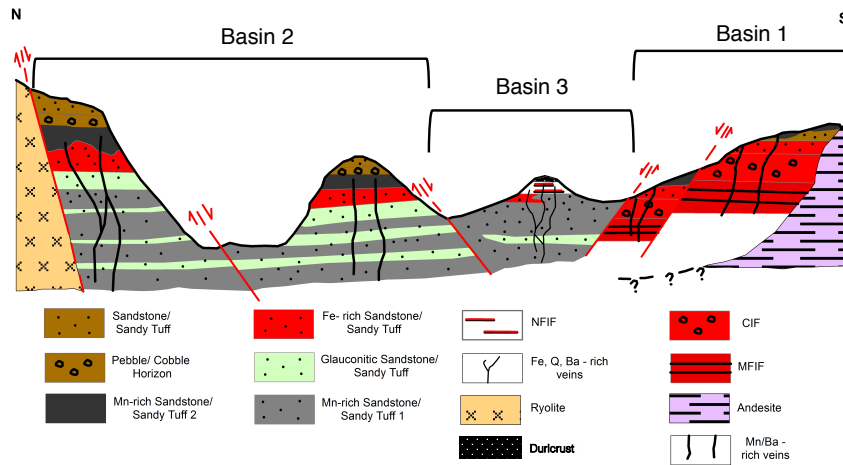
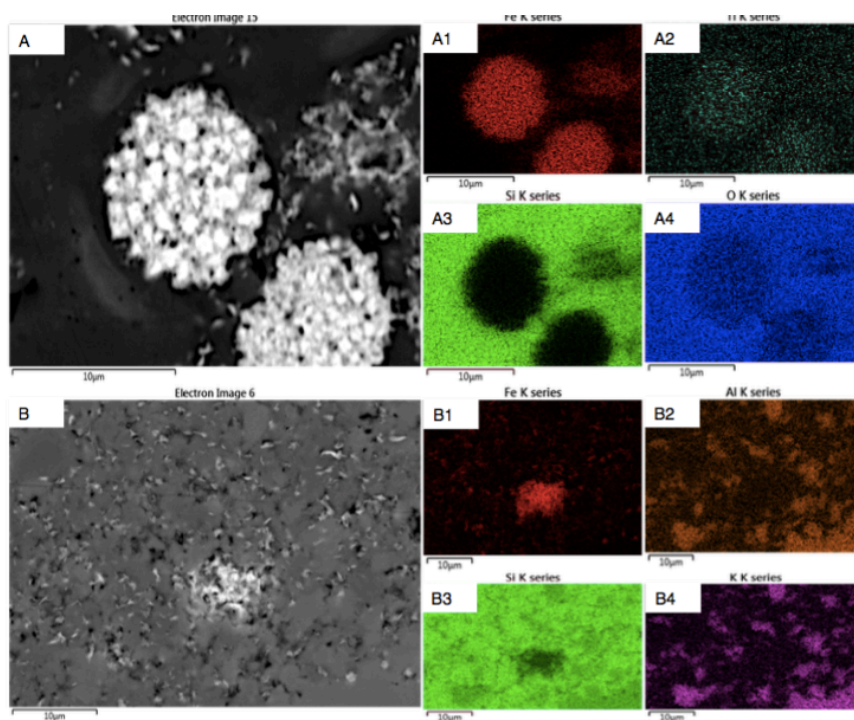


Fig. 2. A generalized north-south stratigraphic map of the ~1 km long CVSB showing interpreted geology, lithology, main faults and how they relate to the iron and manganese formations, in support of a three-basin hypothesis. Not drawn to scale. Four types of iron-rich sedimentary rocks occur in the CVSB. These include the iron-rich sandstones, the iron-Mn-rich sandstones, the conglomerate hosted iron formation (CIF) and the MFIF and NFIF formations that are depositionally and chemically distinct from the sandstone deposits.



1543

1544 Fig. 3. EDS-electron micrograph showing Fe-rich mineral phases in a Si-rich matrix
 1545 from the MFIF. The bright colors correspond to the analysed elements. (A),
 1546 framboidal hematite particles. A1-A4, elemental compositions of the framboidal
 1547 particles in A. (B), Dispersed fluffy Fe-rich mineral grains. B1-B4, corresponding
 1548 elements associated with the micrograph in panel A
 1549

Ernest Chi Fru 5/4/2018 04:45
 Deleted: u

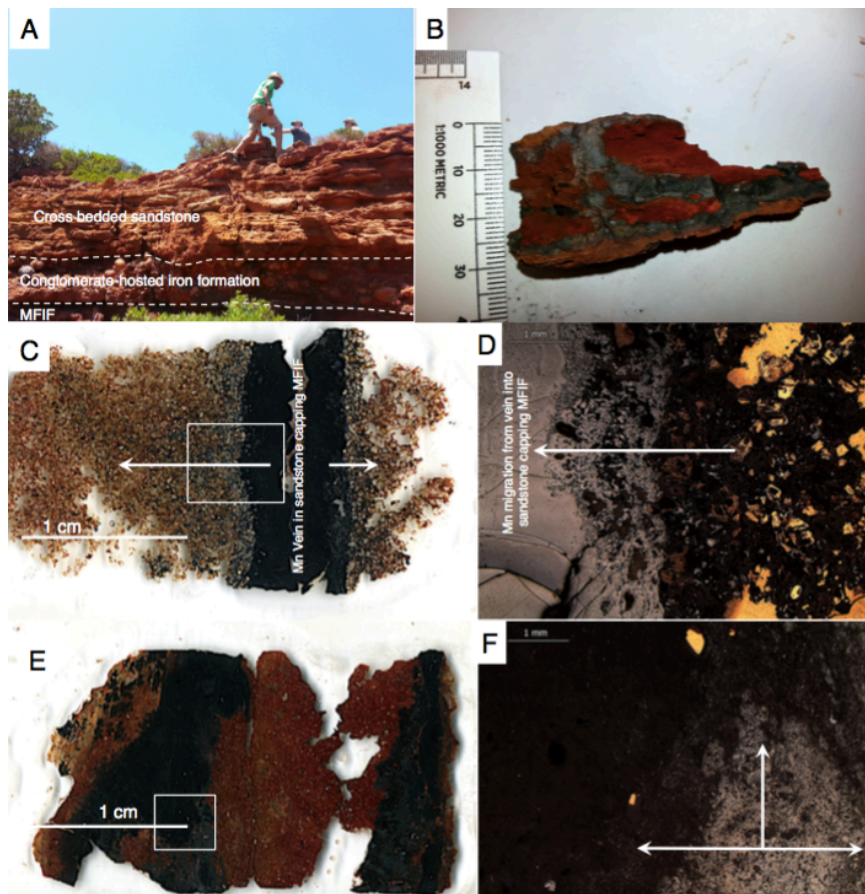


Fig. 4. Sedimentary profile, thin section scans and optical microscope images of the MFIF. (A), Field photo showing the sedimentary profile of the MFIF characterized by the overlying sandstone cap. (B), Photograph showing black diffused Mn-rich bands near the base of the MFIF. (C), Scanned image of thin section showing a black Mn-rich vein in the overlying MFIF sandstone showing a gradient of Mn migrating into the sandstone matrix (white arrows). (D), Light microscopy images showing details in panel C. (E), Scanned image of an MFIF thin section showing black Mn bands migration into a red iron-rich background. (F), Amplified light microscope image showing gray Mn layers migrating into a black Fe-rich matrix. White arrows show direction of movement. Boxes in C and E are amplified in D and F.

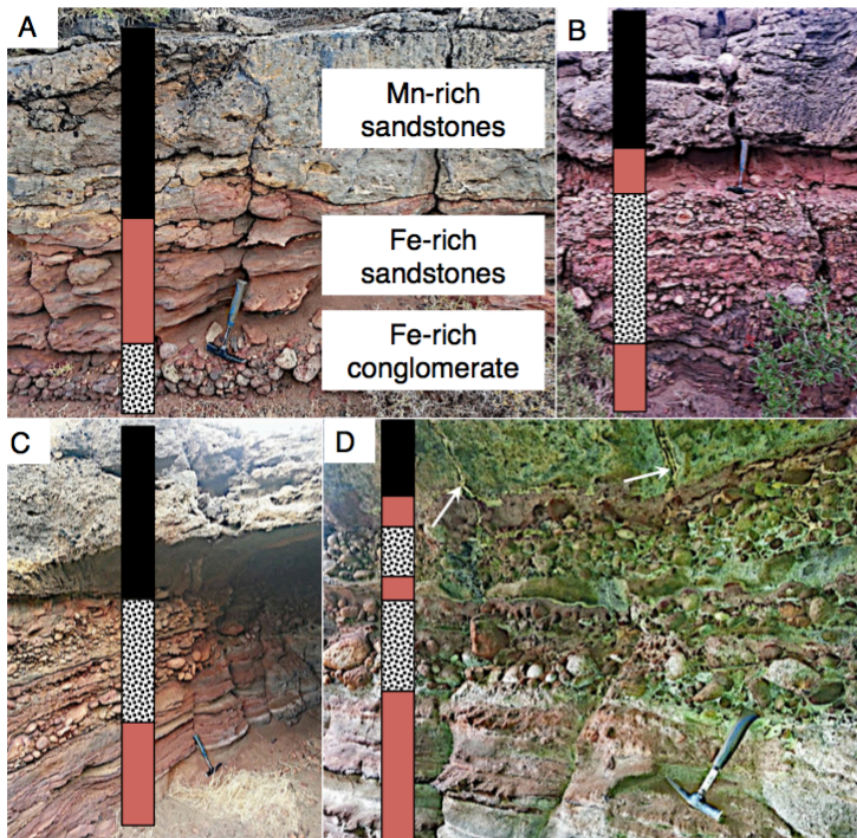


Fig. 5. Sedimentary sequence overlying the MFIF, consisting of thin (<0.5 m) polymictic andesite-dacite cobble-pebble, and sandstone-sandy tuff pebble, and Fe-rich conglomerate facies overlain by thinly laminated Fe-rich sandstone beds. This vertical sequence is interpreted to represent a progressively deeper water environment up the sequence (A), for reasons including sea level rise due to tectonic subsidence. The multiple cycles in B-D suggest potential episodes of sea level change. Arrows in D show hydrothermal feeder veins feeding the overlying layers. The sequence is overlain by a thin package of parallel and cross-bedded Mn-sandstone cap.

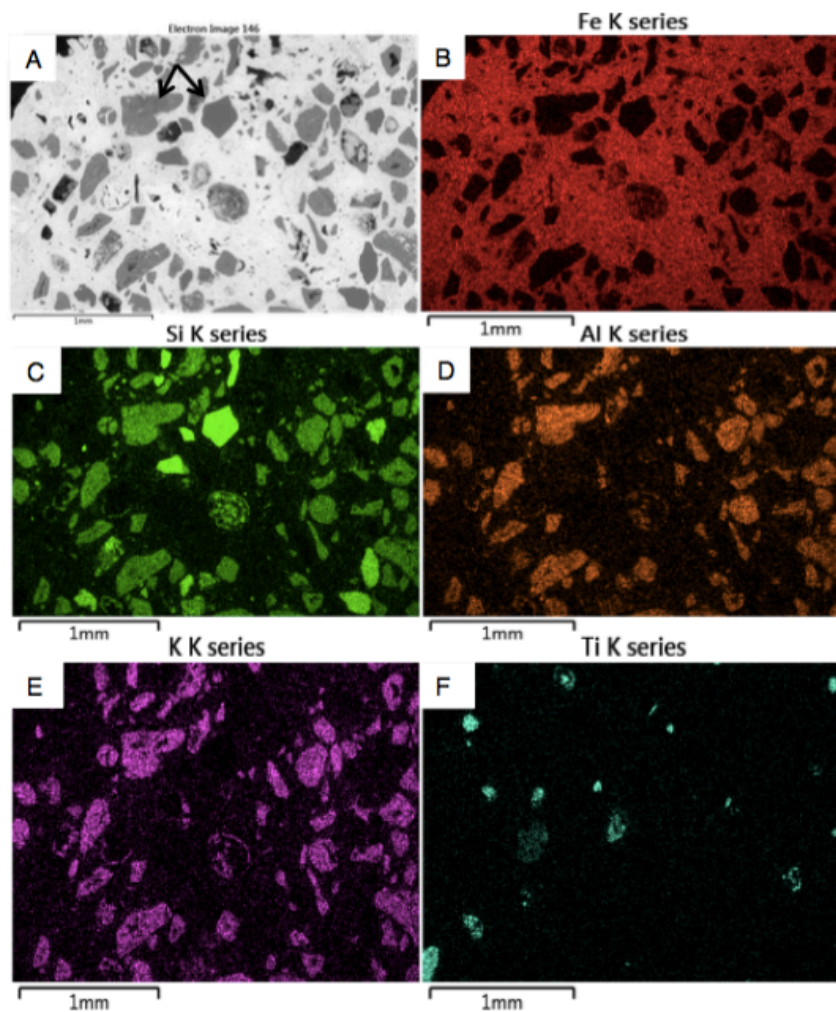
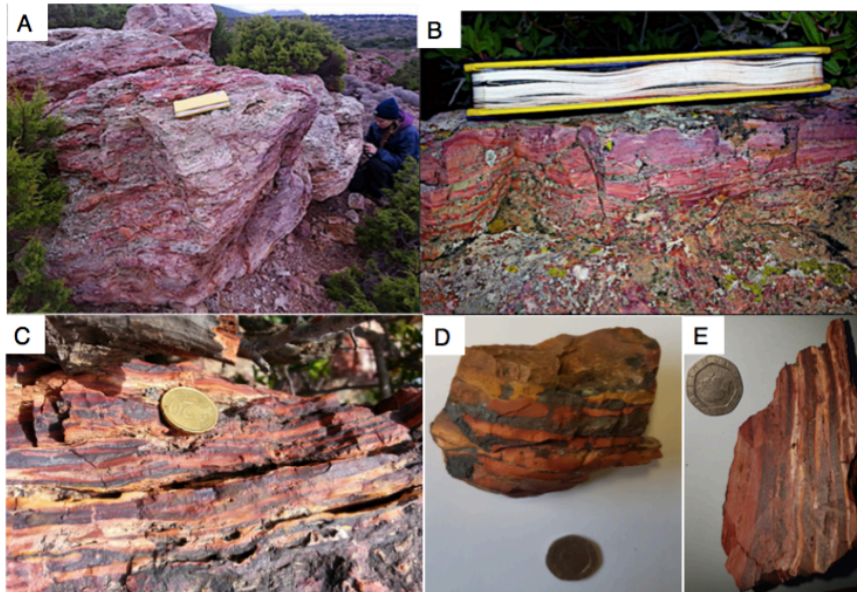


Fig. 6. Scanning electron microscope micrograph showing the chemical composition of volcaniclast (arrows in A) and the iron cement of the conglomerate hosted IF (CIF) overlying the MFIF.



1581

1582 Fig. 7. Examples of the NFIF banded iron rocks. (A-C), Field photographs. (D),
 1583 Handheld banded Fe sample. (E), Sawn NFIF sample with laminated Fe-rich bands
 1584 alternating with Si-rich bands.
 1585

1586

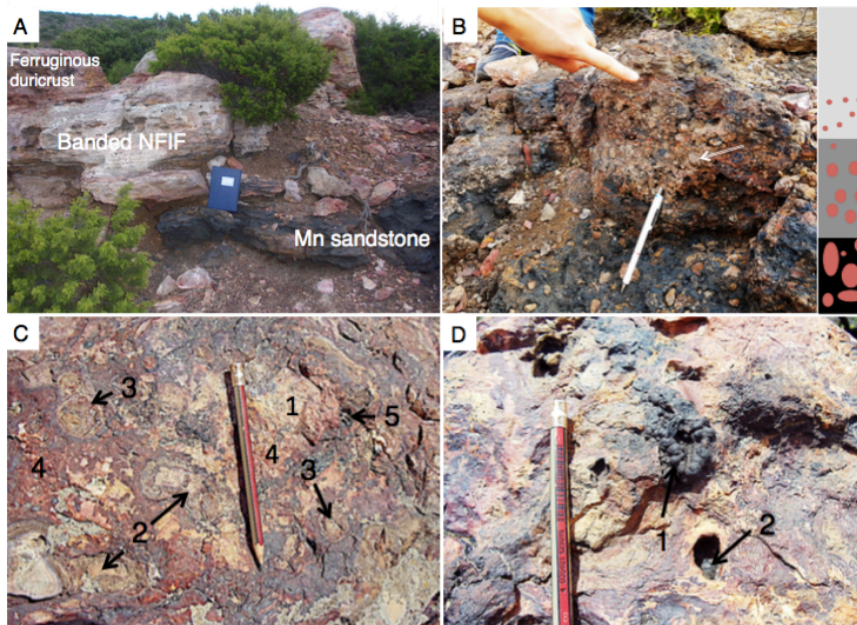
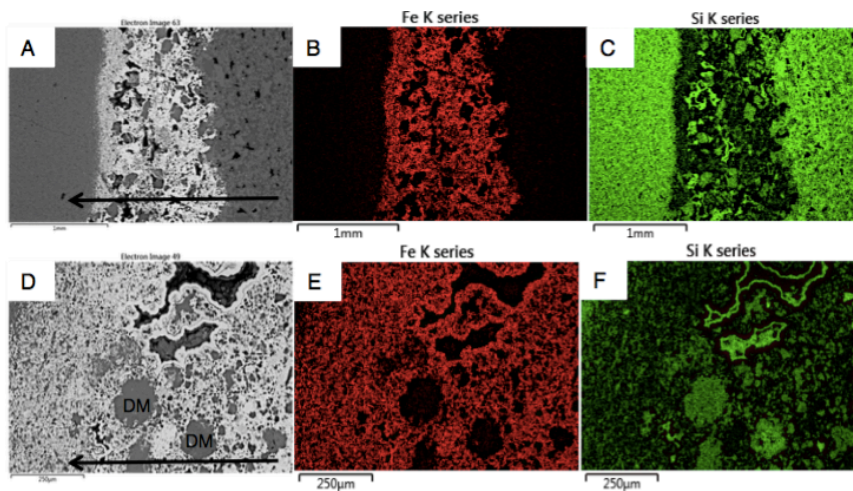


Fig. 8. Field sedimentology and stratigraphy of Section B sequence, host to the NFIF. (A), Sharp boundary between lower Mn sandstone and unconformably overlying NFIF capped by a ferruginous duricrust. (B), Sandstone-sandy tuff pebble to gravel conglomerate facies, showing an upward fining character, locally overlies the Mn sandstone bed and capped by a sharp erosional contact with the overlying NFIF. The tip of the pen (7 cm long) rests on late blue-black Mn oxide overprint. (C), Ferruginous duricrust made up of lithic fragments composed of (1) Fe-nodules (2) and Fe-concretions (3) in a hematite-rich matrix (4). (D), Matrix dissolution resulting in vermiform Mn nodules (1) and cavity black Mn oxide (2) infillings, post-dating the ferruginous duricrust formation.



1600

1601 Fig. 9. EDS-electron micrograph showing major elemental composition of typical Fe
 1602 bands alternating with Si-rich layers in the NFIF. Volcanoclastic detritus mostly
 1603 present in the Fe-rich bands, suggests precipitation during active submarine
 1604 volcanism. To the contrary, the Si-rich band grains that are of a homogenous fine size
 1605 composition and lacking volcanoclast, suggest deposition during intervals of minimal
 1606 volcanic activity. Arrows in A and B depict the direction of sedimentation, seen to
 1607 proceed from an Fe-rich matrix mixed with large grains of volcanoclastic detritus
 1608 (DM) to one composed essentially of very fine-grained Fe particles before
 1609 transitioning into the very fine-grained Si-rich layer. An upward fining of the
 1610 volcanoclastic particles in the Fe-rich layers transitions from one made up of
 1611 volcanoclastic debris and hematite, to a mainly thin hematite-rich horizon at the top of
 1612 this mixed layer (see supplementary Figs 8-11 for details). This concurrent occurrence
 1613 of volcanoclast and Fe oxides, combined with the upward fining nature of the Fe-rich
 1614 layers, suggest the release and oxidation of Fe(II) coincided with the settling of
 1615 hydrothermal debris resulting from the introduction of enormous amount of reduced
 1616 materials into the water column. The Fe-rich layer ceased forming as
 1617 hydrothermal/volcanic release of Fe subsided, followed by deposition of the Si-rich
 1618 layer. This repetitive cycle of events is observed for tens of metres laterally and
 1619 vertically, stressing that the layers are not single isolated or post-depositional
 1620 replacement events, but chemical precipitates that sequentially sedimented out of the
 1621 water column. Red color in B and C depict Fe and green in C and F, Si.

1622

1623

Ernest Chi Fru 5/4/2018 04:45

Deleted: u

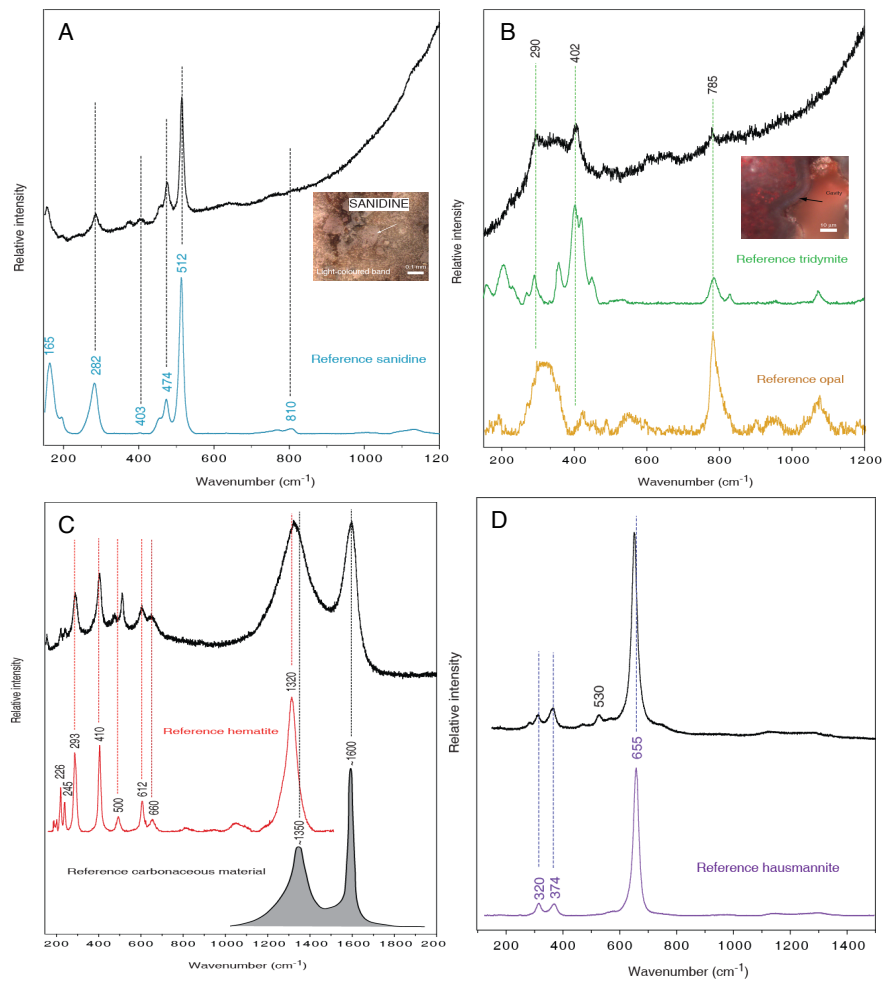


Fig. 10. Raman spectroscopy of the Fe-rich and/or Si-rich bands from NFIF.

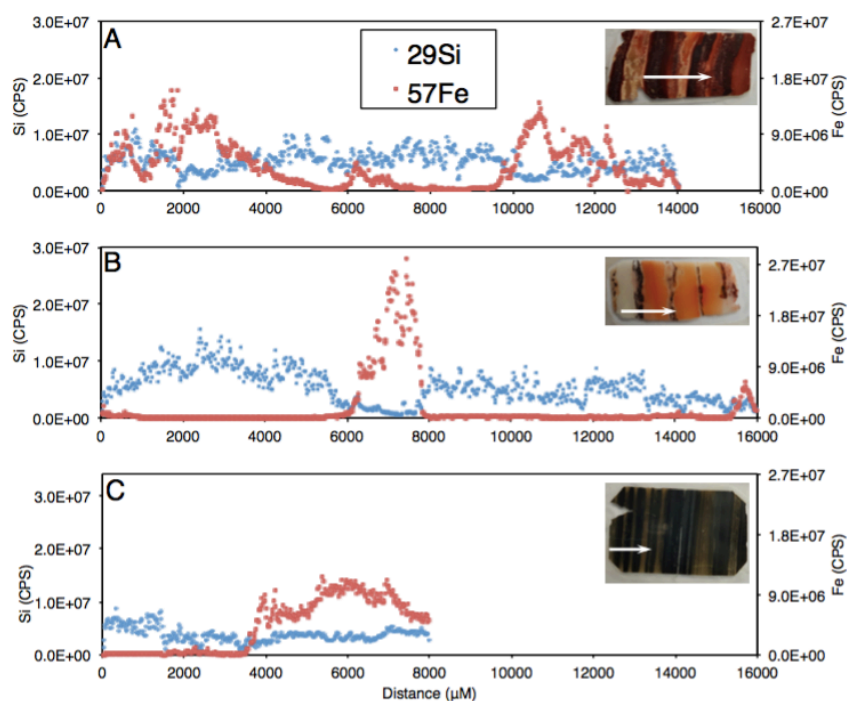


Fig. 11. Fluctuation in Si and Fe content measured by in situ laser ablation ICP-MS analysis. (A), Milos BIF-type rock with evenly distributed Si and Fe rich bands. (B), Milos BIF type rock with wide Si-rich (whitish-brownish strips) and narrow Fe-rich bands (dark strips). (C), An example for the 2.5 Ga Kuruman BIF. Insets are analyzed thin sections. For scale, each thin section is ≈ 3.3 cm long, in the direction of the arrows indicating the area analyzed.

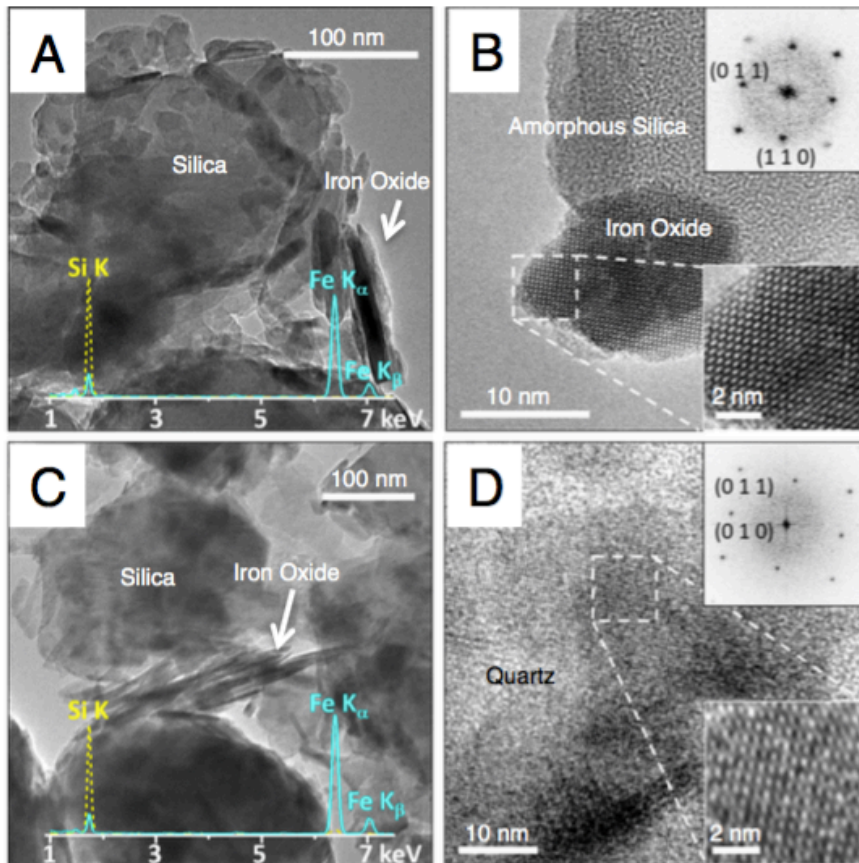


Fig. 12. TEM characterization of an NFIF and MFIF specimen. (A) lower magnification MFIF TEM-BF micrograph. (B) High resolution micrograph of NFIF showing amorphous Si and Fe oxide crystalline lattice structures. Insets highlight a hematite particle viewed from the [1-11] axis (Rhombohedral lattice). (C) Lower magnification MFIF TEM-BF image. (D) High resolution images of MFIF showing crystalline quartz and iron oxide crystalline lattice structures. Insets in (D) show a quartz crystal viewed from the [100] axis. Both samples contain silica with a few hundred nm particle size, and smaller needle-like iron oxide particles. Spectral lines in panels (A) and (C) are X-ray Energy Dispersive elemental profiles of the individual Fe and Si mineral phases.

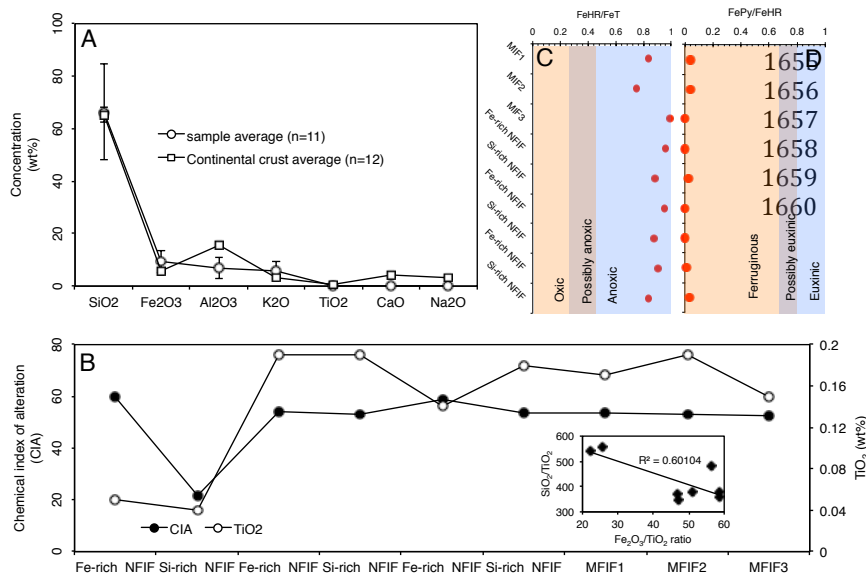


Fig. 13. Bulk average concentrations of major trace elements, chemical weathering indices and reconstructed redox depositional conditions for typical MFIF and the Fe/Si-rich NFIF and for the sawn rock sample in Figure 7E. (A), Relationship between average major trace element content and average continental crust (Rudnick and Gao, 2003). (B), Chemical Index of Alteration (CIA). Inset, relationship between SiO₂ and Fe₂O₃. (C) Highly reactive Fe (FeHR) to Total Fe ratio (FeT). (D) Pyrite to FeHR ratio.

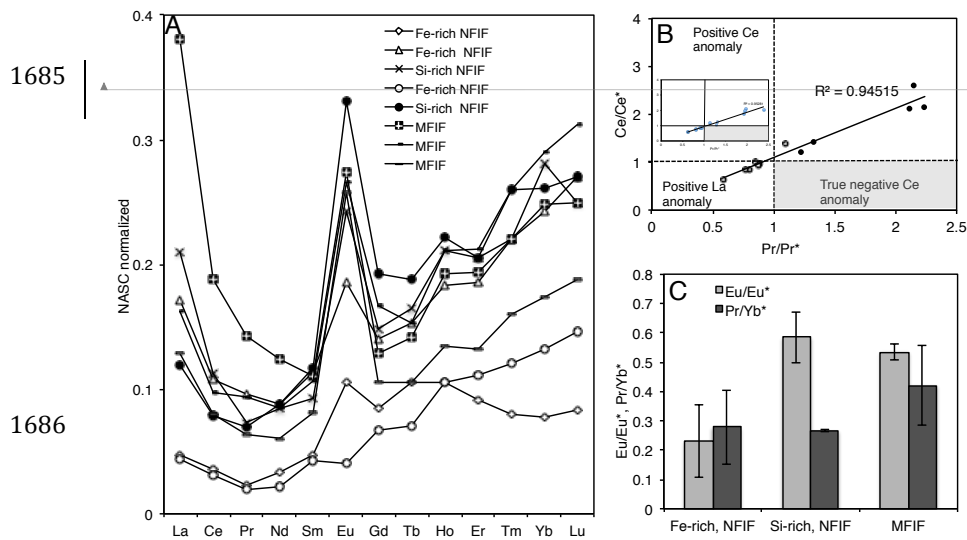
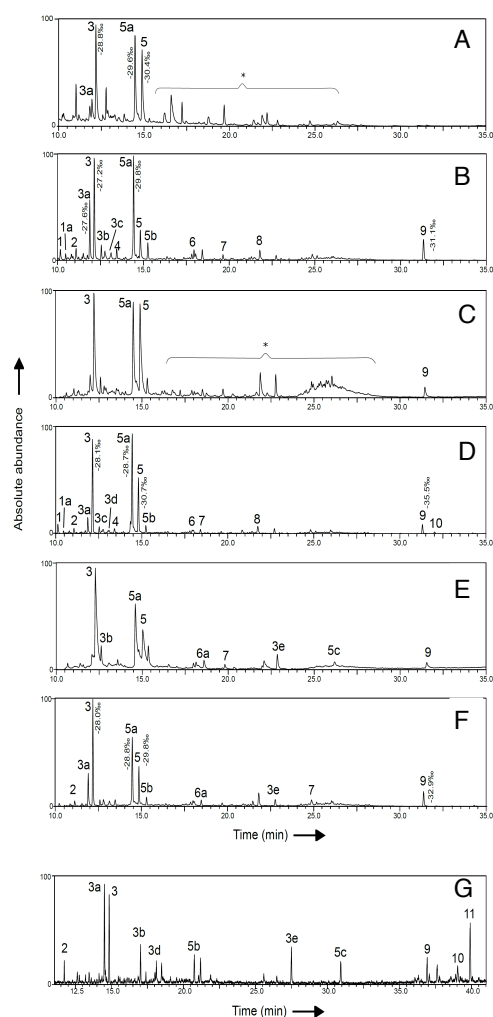


Fig. 14. Rare earth element (REE) distribution in samples and calculated Ce and Eu anomalies for NFIF bands and MFIF. (A), NASC normalized REE distribution in various rock facies. (B), Ce anomalies. (C), Eu anomalies and light REE (LREE) vs. heavy REE (HREE) ratio in the NFIF bands and MFIF. Similar trends were reproduced for Post Archean Australian Shale (PAAS) normalized REE (McLennan, 1989; Bau and Dulski, 1986), exemplified by the inset in B.



1693

1694 Fig. 15. GC/MS chromatogram sections of total lipid extracts of the BIF-type rocks
 1695 (A-F). Data are for individual bands excised from the sawn rock in Figure 7E. Panel
 1696 G illustrates total lipid extract for the modern shallow submarine hydrothermal
 1697 sediments at Spathi Bay, south east on the coast of Milos Island. Peak values indicate
 1698 the lipid-specific $\delta^{13}\text{C}$ values per mil. Because of the low intensity of the lipids
 1699 recovered, it was not possible to obtain $\delta^{13}\text{C}$ values specific for all peaks. Peaks are
 1700 annotated as; FAME = fatty acid methyl ester; Me = methyl group; TMS =
 1701 trimethylsilyl; TMSE = trimethylsilyl ester. (1) $\text{C}_{14:0}$ FAME, (1a) $\text{C}_{14:0}$ 13Me FAME,
 1702 (2) $\text{C}_{15:0}$ FAME, (3) $\text{C}_{16:0}$ FAME, (3a) $\text{C}_{16:9}$ FAME, (3b) $\text{C}_{16:0}$ TMS, (3c) 10Me $\text{C}_{16:0}$
 1703 FAME, (3d) $\text{C}_{16:9}$ FAME, (3e) $\text{C}_{16:0}$ TMSE, (4) $\text{C}_{17:0}$ TMS, (5) $\text{C}_{18:0}$ FAME, (5a) $\text{C}_{18:9}$

1704 FAME, (5b) C_{18:0} TMS, (5c) C_{18:0} TMSE, (6) C_{19:0} FAME, (6a) C_{19:0} 18Me TMS, (7)
1705 C_{21:0} TMS, (8) C_{22:0} TMS, (9) Cholesterol TMS, (10) Stigmasterol TMS, (11) beta-
1706 Sitosterol (*) contaminants (e.g., phthalates).
1707

1708

1709

1710

1711

1712

1713

1714

1715

1716

1717

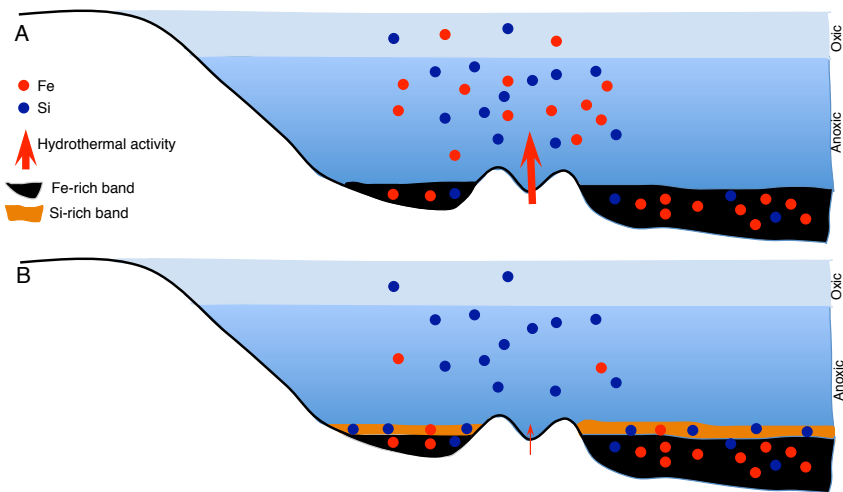
1718

1719

1720

1721

1722



1723

1724 Fig. 16. Conceptual model of the mechanism of band formation of the NFIF, related
 1725 to changes in the intensity of hydrothermal activity and chemical oxidation of Fe(II)
 1726 to Fe(III) in the water column, inferred from the data. See Chi Fru et al. (2013) for a
 1727 biological model for the formation of the MFIF.